



**HAL**  
open science

## Light-activated interlayer contraction in two-dimensional perovskites for high-efficiency solar cells

Wenbin Li, Siraj Sidhik, Boubacar Traore, Reza Asadpour, Jin Hou, Hao Zhang, Austin Fehr, Joseph Essman, Yafei Wang, Justin Hoffman, et al.

### ► To cite this version:

Wenbin Li, Siraj Sidhik, Boubacar Traore, Reza Asadpour, Jin Hou, et al.. Light-activated interlayer contraction in two-dimensional perovskites for high-efficiency solar cells. *Nature Nanotechnology*, 2022, 17 (1), pp.45-52. 10.1038/s41565-021-01010-2 . hal-03441919

**HAL Id: hal-03441919**

**<https://hal.science/hal-03441919>**

Submitted on 17 Feb 2023

**HAL** is a multi-disciplinary open access archive for the deposit and dissemination of scientific research documents, whether they are published or not. The documents may come from teaching and research institutions in France or abroad, or from public or private research centers.

L'archive ouverte pluridisciplinaire **HAL**, est destinée au dépôt et à la diffusion de documents scientifiques de niveau recherche, publiés ou non, émanant des établissements d'enseignement et de recherche français ou étrangers, des laboratoires publics ou privés.



Distributed under a Creative Commons Attribution - NonCommercial 4.0 International License

# Light-activated interlayer contraction in 2D perovskites for high-efficiency solar cells

Wenbin Li<sup>1,2</sup>, Siraj Sidhik<sup>1,5</sup>, Boubacar Traore<sup>3#</sup>, Reza Asadpour<sup>4</sup>, Jin Hou<sup>5</sup>, Hao Zhang<sup>1,2</sup>, Austin Fehr<sup>1</sup>, Joseph Essman<sup>1</sup>, Yafei Wang<sup>1</sup>, Justin Hoffman<sup>6</sup>, Ioannis Spanopoulos<sup>6</sup>, Jared J. Crochet<sup>7</sup>, Esther Tsai<sup>8</sup>, Joseph Strzalka<sup>9</sup>, Claudine Katan<sup>10</sup>, Muhammad A. Alam<sup>4</sup>, Mercouri G. Kanatzidis<sup>6</sup>, Jacky Even<sup>3</sup>, Jean-Christophe Blancon<sup>1\*</sup> and Aditya D. Mohite<sup>1,5\*</sup>

<sup>1</sup>Department of Chemical and Biomolecular Engineering., Rice University, Houston, TX, 77005, USA.

<sup>2</sup>Applied Physics Program, Smalley-Curl Institute, Rice University, Houston, TX, 77005, USA

<sup>3</sup>Univ Rennes, INSA Rennes, CNRS, Institut FOTON - UMR 6082, F-35000 Rennes, France.

<sup>4</sup>School of Electrical and Computer Engineering, Purdue University, West Lafayette, Indiana 47907, USA

<sup>5</sup>Department of Materials Science and NanoEngineering., Rice University, Houston, TX, 77005, USA.

<sup>6</sup>Department of Chemistry and Department of Materials Science and Engineering, Northwestern University, Evanston, IL, 60208, USA.

<sup>7</sup>Los Alamos National Laboratory, Los Alamos, NM, 87545, USA.

<sup>8</sup>Center for Functional Nanomaterials, Brookhaven National Laboratory, Brookhaven, NY, 11973

<sup>9</sup>X-Ray Science Division, Argonne National Laboratory, Argonne, IL 60439, USA.

<sup>10</sup>Univ Rennes, ENSCR, INSA Rennes, CNRS, ISCR (Institut des Sciences Chimiques de Rennes) - UMR 6226, F-35000 Rennes, France

\*Correspondence to: [blanconjc@gmail.com](mailto:blanconjc@gmail.com), [adm4@rice.edu](mailto:adm4@rice.edu)

#Univ Rennes, ENSCR, INSA Rennes, CNRS, ISCR (Institut des Sciences Chimiques de Rennes) -UMR 6226, F-35000 Rennes, France

Understanding and tailoring the physical behavior of halide perovskites under practical environments is critical for designing efficient and durable optoelectronic devices. Here, we report that continuous light illumination leads to >1% contraction in the out-of-plane direction in 2D hybrid perovskites, which is reversible and strongly dependent on the specific superlattice packing. X-ray photoelectron spectroscopy measurements show that constant light illumination results in the accumulation of positive charges in the terminal iodide atoms, thereby enhancing the bonding character of inter-slab I-I interactions across the organic barrier and activating out-of-plane contraction. Correlated charge transport,

**structural and photovoltaic measurements confirm that the onset of the light-induced contraction is synchronized to a three-fold increase in carrier mobility and conductivity, which is consistent with an increase in the electronic band-dispersion predicted by first principles calculations. Flux dependent space charge limited current measurement reveals that light-induced interlayer contraction activates interlayer charge transport. The enhanced charge transport boosts the photovoltaic efficiency of 2D perovskite solar cells up to 18.3% by increasing its fill factor and open circuit voltage.**

Two-dimensional (2D) hybrid perovskites have recently emerged as solution-processed semiconductors with unique physical properties, which offer opportunities for optoelectronics, spintronics, and energy conversion technologies of the future.<sup>1-5</sup> Most of the reported structures are formed by the chemical assembly of stacks of nanometer-thick hybrid perovskite layers, separated by bulky insulating organic spacer cations such as alkylammonium or thienyl-, phenyl-, and cyclohexyl-based monovalent cations and adopt a so-called Ruddlesden-Popper (RP) phase.<sup>6-8</sup> The composition of the organic moieties and the perovskite layer thickness (expressed by the  $n$ -value in the chemical formula  $L_2A_{n-1}B_nX_{3n+1}$  where L is the organic monovalent spacer, A is methylammonium (MA), formamidinium (FA) or Cs, B is a divalent metal such as Pb or Sn, and X is a halide – I, Br, or Cl) define the crystal phase, structural, mechanical, electronic and optical properties of resulting 2D perovskites.<sup>8-17</sup>

Recent work by Kanatzidis and co-workers demonstrated that using spacer dications, such as piperidinium (4AMP) or a mixture of small cations such as guanidinium (GA) and MA instead of the well-known butylammonium (BA) leads to the formation of 2D hybrid perovskites with different crystal structures such as Dion-Jacobson (DJ) and Alternating Cation Interlayer (ACI), in which the interlayer distance is much smaller than the well-studied Ruddlesden-Popper (RP).<sup>7,8,18,19</sup> For iodide perovskites, which are the most suitable for single-junction solar cells, the I-I distance can be as small as 4 Å compared to 7 Å with BA. Moreover, the stacking of the perovskite layers and the use of the short cation (4AMP) in the DJ structure imposes a perfectly eclipsed alignment on the layer stacking, resulting in weak but significant electronic coupling between the iodide atoms directly facing each other across the organic interlayer.<sup>18,19</sup> Due to the recombination of carriers at the organic-inorganic interfaces and imperfect crystal packing in thin films, the 2D hybrid perovskites exhibit inferior charge transport properties as compared to their 3D counterparts, which has a direct impact on the efficiency of photovoltaic devices.<sup>12,20,21</sup>

Tailoring interlayer interactions by using suitable organic cations or external mechanical stress has been predicted to enhance the electronic coupling between perovskite layers across the organic spacer and significantly enhance the charge transport in 2D hybrid perovskites.<sup>9,22–27</sup> This approach would enable the synthesis of thicker films (>400 nm like 3D), increase the absorption, and bridge the efficiency gap between the 2D and 3D perovskites.<sup>20</sup>

Here, we show that continuous illumination of the DJ and ACI 2D hybrid perovskites results in a lattice contraction with a 0.4% decrease in the lattice parameter of the perovskite layer plane (in-plane) direction and >1% decrease in the out-of-plane direction lattice parameter. In-situ X-ray photo-electron spectroscopy measurements performed on single-crystals and thin-films under continuous illumination reveal that upon illumination, the iodide atoms become electron poor (more positively charged or oxidized), which triggers an enhancement of the I-I interactions across an organic barrier. This decreases the effective interlayer distance and results in a 3-fold, step-like increase in the charge carrier mobility. Importantly, the abrupt change in the mobility is perfectly in sync with the onset of lattice contraction in the in-situ device GIWAXS. Furthermore, light-intensity dependent GIWAXS and mobility measurements elucidate a percolation-based mechanism, which explains the 3-fold increase in mobility and the observed timescale of the light-induced changes and the subsequent relaxation. Theoretical calculations reveal that the localization of holes on the iodine atoms results in larger electronic dispersion along the stacking axis, which is consistent with our experimental observation of enhanced charge transport. The improved charge transport results in a large increase in the efficiency of a DJ-based photovoltaic device from 15.6% to 18.3%, mainly due to improved charge collection, reflected as an increase in the fill factor and open circuit voltage of the solar cell.

### **Structural characterization of 2D perovskite under light**

The 2D perovskites were exposed to the light from a solar simulator (AM 1.5G) while their structure was monitored using grazing incident wide angle X-ray scattering (GIWAXS) as a function of illumination time (Fig. 1a). Figure 1a illustrates the experimental setup and the corresponding GIWAXS pattern of Dion-Jacobson 4AMP-MA<sub>2</sub>Pb<sub>3</sub>I<sub>10</sub> (DJ *n*=3) perovskite crystal powders, which shows concentric rings with constant *q*-radius corresponding to the Bragg reflections of DJ *n*=3 lattice planes identified by their Miller indices (Fig. 1b, filled curve; structure of the DJ *n*=3 in Fig. 1c; and complete *q*-range is shown in Supplementary Fig. 1). Under constant light illumination, all the diffraction peaks decrease in intensity and shift to higher *q* values (Fig.

1b). The light-induced increase in the  $q$ -value of the diffraction is attributed to a continuous and reversible lattice contraction in all directions. The lattice contraction corresponds to a 2% reduction in the volume of the lattice unit cell after 51 minutes of illumination (Supplementary Table 1). Detailed analysis of the evolution of the diffraction peaks (see results for the 300 and 011 peaks in Supplementary Fig. 2a, b) yields a monotonic decrease of the out-of-plane and in-plane lattice parameters (Fig. 1d and Supplementary Fig. 2). After 51 minutes of illumination, we observed a contraction of the lattice by 1.0% (23.12 to 22.90 Å) and 0.56% (8.847 to 8.803 Å) in the out-of-plane and in-plane directions, respectively (Fig. 1e). These relative changes in the lattice parameter values **over time**, which can be interpreted as the normal strain induced in the lattice by light, reveal that the light-induced lattice contraction effect is significantly stronger in the direction of the stacking axis (out-of-plane) as compared to the in-plane direction. In addition, we also observed an increase in the intensity of the diffraction peaks stemming from a new polymorph of the DJ  $n=3$  (labeled “P” in Supplementary Fig. 2), which exhibits a first order contraction of the lattice volume by about 7% as compared to the nominal DJ  $n=3$  phase before illumination. However, we emphasize that the latter effect was exclusively observed only on powder samples and not present in DJ  $n=3$  single crystals (Fig. 1f) or thin films integrated into solar cells (Fig. 5). These results imply that sample preparation and morphology as well as edges and surfaces might play an important role in the manifestation of the contracted polymorph. In contrast, the continuous and reversible light-induced lattice contraction of the original perovskite phase is an intrinsic phenomenon observed for all types of samples and is a bulk property.

Next, to verify that the light-activated contraction phenomena reported in Fig. 1 is purely light induced, we performed the following analysis. First, we confirmed that our samples do not exhibit any light-induced irreversible degradation, as the total intensity of the GIWAXS patterns remained constant during light illumination (Supplementary Fig. 2c) and the light-induced changes are reversible after placing the 2D perovskites in the dark for several hours (Fig. 1b and Supplementary Fig. 2 a, b). Second, we excluded the possibility that the observed lattice contractions were due to heating by investigated the structural changes in DJ  $n=3$  as a function of temperature in the dark. The temperature dependence as illustrated in Fig. 1g (and Supplementary Fig. 3) showed that the diffraction peaks shift to smaller  $q$  values with increasing temperature, which is a clear indication of a lattice expansion and is opposite to the light-induced results reported in Fig. 1b and d. In addition, above  $-40^{\circ}\text{C}$  we observed the coexistence of the original

phase and the new polymorph all the way up to 80 °C (Supplementary Fig. 3). We note that coexistence between polymorphs, including phases with the same space groups, have been observed in 2D perovskites and recent studies suggest that their transformation can be tuned by temperature and pressure.<sup>9,24,25</sup>

To understand how the light-induced structural changes observed in DJ  $n=3$  depend on its specific crystal structure we investigated two other types of 2D perovskite structures (Fig. 2a): the alternating cation (ACI) perovskites ( $\text{GAMA}_3\text{Pb}_3\text{I}_{10}$  ;  $n=3$  and  $\text{GAMA}_2\text{Pb}_2\text{I}_7$   $n=2$  in Supplementary Fig. 4), and the Ruddlesden-Popper (RP) perovskite ( $\text{BA}_2\text{MA}_3\text{Pb}_3\text{I}_{10}$  ;  $n=3$  in Supplementary Fig 5).<sup>7,19</sup> We observed that both the ACI  $n=2$  and  $n=3$  showed light-induced structural changes similar to the DJ  $n=3$ . Surprisingly, the RP  $n=3$  exhibited no measurable structural changes after one hour of illumination. Figure 2b presents a quantitative comparison of both the in-plane and out-of-plane light-induced normal strain under constant illumination in all samples (also summarized in Supplementary Table 1). The in-plane compressive strain showed a similar trend in both the DJ and ACI samples and reached values between -0.40 and -0.50 % respectively, after 51 minutes of illumination. On the other hand, the out-of-plane strain amplitude increased at a much faster rate under continuous illumination and reached values between -0.6 and -1.0 %, with DJ  $n=3$  exhibiting the largest compressive strain and ACI  $n=3$  the smallest one. We note that while the light did not induce any structural changes in the RP  $n=3$ , we observed a lattice expansion upon heating in the RP samples in the dark (Supplementary Fig. 3), which further confirmed that light-induced temperature effects can be ignored in our in-situ GIWAXS experiments. Finally, similar to the DJ  $n=3$ , both the ACI and RP 2D perovskites exhibited an increase in the polymorphic phase as a function of increasing temperature. These measurements suggest that there exists a correlation between the different structural phases of 2D perovskite and the effect of light induced contraction.

### **Mechanism of light-activated interlayer contraction**

To understand the mechanistic origin of the light-induced lattice contraction, we performed X-ray photoelectron spectroscopy (XPS) measurements before and after light exposure on mm-sized DJ and RP single crystals (Fig. 2c, d). This allowed us to directly probe the chemical bonding states of the Pb 4f and I 3d electron core levels (Fig. 2c, left and right, respectively). Our results showed a clear blue shift in the binding energies of both iodide and lead atoms in the DJ sample. The blue shift in the bonding states is indicative of the loss of electrons (or oxidation) of the iodide

atoms. The more positively charged iodides across the interlayer can undergo an oxidative coupling, which results in the out-of-plane contraction and a decrease in the effective interlayer distance. We note that this mechanism is akin to the well-known formation of polyiodides, specifically oxidative coupling of iodide ions to create  $I_n^{1-}$  molecular weakly bound polyiodide oligomers.<sup>30</sup> A similar shift was also observed for Pb core levels; however, the shift in energy for the iodide core levels was larger ( $0.25 \pm .002$  eV vs  $0.20 \pm .006$  eV, iodide versus lead respectively). This is consistent with the fact that electrons on the Pb bonding states are quickly delocalized and as a result experience a secondary oxidative environment.<sup>28,29</sup> In sharp contrast to the DJ perovskite, the RP system exhibited no measurable shift in the binding energies under light exposure (Figure 2d). Moreover, the 3D structure resulted in a red shift in Pb and I core levels, consistent with previous reports (Supplementary Fig. 6a,b)<sup>30</sup> and opposite to the trend observed for 2D perovskites. These XPS trends measurements clearly imply that light-induced out-of-plane contraction is correlated to the interlayer iodide interactions in DJ and ACI 2D perovskites in which the interlayer distance is the shortest.

Previous reports claim that the orbital nature of the valence band in the perovskites is antibonding in character and has a significant contribution from the  $6s^2$  states of the  $Pb^{2+}$  atoms as well as the filled p states from iodine atoms.<sup>14,18,27</sup> Therefore, light excitation across the bandgap involves the creation of holes via the depopulation of antibonding states with both Pb and I contributions in the valence band. Because of the proximity of the adjacent slabs enabled by the very short spacer cations, some holes can get trapped through the enhanced I-I weakly bonding interactions across the slabs, resulting in contraction along the out-of-plane direction. Moreover, a key requirement for this mechanism to be activated is that the I-I distance across the slabs must be short, therefore, this effect of light-activated interlayer contraction is observed only in DJ and ACI perovskite.

To gain a deeper insight into the mechanism proposed by the in-situ XPS measurements and to understand the impact of the out-of-plane light-induced contraction on the band-structure, we performed first principles calculations based on density functional theory (DFT) for 2D perovskites under various charged states (modeling details in methods section). Our model confirmed that the lattice contraction stems from the accumulation of photogenerated holes in the bulk, which leads to a compressive strain of the perovskite superlattice through a decrease of the interlayer spacing (Fig 3 and Supplementary Fig. 6c, d). DFT calculation also predicts that the

light-induced effects are more prominent in the DJ versus ACI, which confirms the fact that iodide interactions are stronger in the shorter interlayer iodide distance DJ perovskite (4.12Å) compared to the ACI perovskite (4.46Å) (Supplementary Information Table 3 and 5). Furthermore, to mimic the enhancement of the inter-slab I-I bonds by the accumulation of holes on the iodides, we calculated the electronic band structure of the DJ perovskite as a function of positive charge carrier (hole) injection (Fig. 3c). Our simulation shows that after one- to two-hole injections, the curvature at the valance band maxima and conduction band minima exhibited a larger dispersion along the octahedra stacking axis ( $\Gamma - X$ ) compared to the neutral case. This dispersion implies that a significant change in the charge carrier properties can be expected. Finally, we note that a positively charged RP perovskite is predicted to undergo a vertical lattice contraction according to DFT calculations, therefore confirming that the absence of lattice contraction and XPS shifts (Figure 2 b, d) is attributed to the lack of positive charge accumulation in the case of RP phase 2D perovskites. This is reasonable because such accumulation requires the existence of short I-I in the structure to begin with. In fact, two pathways, which can efficiently drive away the photo-generated charge carriers in the bulk of RP perovskites are via low-energy states at their edge surfaces, or by the quick formation of Wannier excitons.<sup>31-33</sup>

### **In-situ transport and device measurements**

Motivated by the DFT band-structure calculations, which predict an increase in band-dispersion upon light-induced contraction in the out-of-plane direction, the next logical step was to quantify its impact on the electronic transport. We conducted in-situ space charge limited current (SCLC) measurements under continuous light illumination (Fig. 3d) by fabricating an electron only device by sandwiching a DJ  $n=3$  2D perovskite thin-film between ITO/SnO<sub>2</sub> and C<sub>60</sub>/Cu (fabrication process in the methods section). We first measured the current-voltage (J-V) characteristics of the device in the dark and observed two regimes (Supplementary Fig. 7a). At low voltages, the J-V curve showed a linear dependence ( $J = \alpha V^1$ ) indicating an Ohmic response. At higher voltages ( $> 3V$ ), the linear response shifted towards a nonlinear regime ( $J = \alpha V^3$ ) signaling a transition to a trap-filled limited region (TFL) (details of the fitting are in the Methods). These results are in good agreement with previous reports.<sup>21,34,35</sup> Next, we exposed the device to constant 1-sun light illumination. A new sublinear response ( $J = \alpha V^{1/2}$ ) was observed in J-V curve between the ohmic and TFL regions (Supplementary Fig 7b). We attribute this to the space charge

limited photocurrent regime, where generated photocarrier and injected free carrier concentrations exceed the background charge carrier concentration and accumulate at one of the interfaces to create a space charge build-up.<sup>36,37</sup> Nevertheless, we directly monitored the JV trace of the electron device under light illumination which is shown in figure 3d. We observed a sudden jump in the JV trace upon 10 minutes of light illumination. The conductivity analysis (extracted from the fit in ohmic region) indicates that after 10 minutes of light illumination, a sigmoidal increase of conductivity occurred, from  $50 \times 10^{-9}$  (S/cm) to  $120 \times 10^{-9}$  (S/cm) (Fig. 4b). Similarly, the carrier mobility increased from  $0.5 \text{ cm}^2/\text{V}\cdot\text{s}$  to  $1.5 \text{ cm}^2/\text{V}\cdot\text{s}$  after 10 mins of light soaking (Fig. 4c). These results suggest that the charge transport is significantly enhanced within a short time of 10 minutes, even though the effect of light-induced contraction had just initiated. The improvement in the charge transport properties is consistent with the increase in the out-of-plane dispersion predicted by DFT simulations and is indicative of the activation of the interlayer transport pathway. In fact, recent work by Ma et. al. has shown that when reducing the length of the organic spacer cation, a new interlayer transport channel is created.<sup>38</sup>

To gain a deeper insight into the correlation between the light-induced contraction and the enhancement in charge transport, we performed light intensity dependent GIWAXS and SCLC measurements described below. GIWAXS measurements were performed on DJ n=3 powders using two illumination intensities, 0.4 and 1.0 sun (Supplementary Fig. 8a). Similar to the 1-sun measurements shown in Fig. 1, lower light intensity illumination induces an anisotropic contraction for the out-of-plane and in-plane diffraction planes. However, we find that at 0.4 suns, the magnitude of the strain was lower in both directions with -0.24% compressive strain in the out-of-plane direction and -0.16% strain in the in-plane direction. Moreover, the slope of the light-induced strain for both the directions was smaller than the 1-Sun case. Next, to build on our intensity dependent GIWAXS, we performed a flux dependent SCLC measurement on an electron-only device. Our SCLC results reveal several interesting phenomena, (i) a sudden sigmoidal variation (a constant lower and upper limit) of the mobility as a function of time under constant light illumination at different light intensities (Fig. 4d), (ii) 3-fold increase of the mobility, which is independent of the light intensity (Fig. 4d), (iii) inverse relationship between the time of nonlinear increase and the flux of light illumination (Fig. 4e). Analogous to the classical percolation theory for electrical conductivity in inhomogeneous medium, the transition between low and high conductive states occurs when a percolation threshold due to doping.<sup>39,40</sup> We propose

that our system follows an equivalent concept in which the method of doping is the trapping/localization of photogenerated holes at the iodide sites (threshold).

The percolation model is explained in detail in the supplementary discussions. In summary, our results on the intensity dependent GIWAX and SCLC measurements combined with a percolation model elucidates that there is a threshold number of iodide sites that need to be filled by the photogenerated holes to activate light-induced contraction and the subsequent increase in mobility (Fig. 4c). Furthermore, we performed a GIWAXS measurement on DJ n=3 perovskite thin film to probe the orientation of the grains (Supplementary Fig. 9a). The diffraction results showed that DJ perovskite thin-film exhibits a mixed orientation with mostly preferential vertical orientation (perpendicular to the substrate) and some horizontal orientation along the in-plane direction (parallel to the substrate). This indicates that before light illumination a large fraction of the photogenerated carriers is scattered off by the organic spacer cation due to the mixed arrangements of the inorganic perovskite layers.<sup>2</sup> However, when the number of trapped photogenerated holes equals to the percolation threshold, interlayer transport is activated by the interlayer contraction (Fig. 4g). This enhances the overall mobility and can be seen by the percolation transition in the SCLC measurement.

In order to directly probe the impact of light-induced contraction on the performance of photovoltaic devices, we performed correlated structural (GIWAXS) measurements on planar, p-i-n solar cells using DJ n=3 as the 2D perovskite in-operando. (Fig. 5a-c and Supplementary Fig. 9). Figure 5c shows the effective interlayer distance extracted from the GIWAXS measurements as a function of light illumination time. Similar to the single crystals and powder samples, thin-films of DJ n=3 also exhibit a light-induced anisotropic compressive strain resulting in the contraction of the effective interlayer distance. We observed a step-like increase in the open-circuit voltage ( $V_{oc}$ ) and fill factor (FF) after 10 minutes illumination (Fig. 5b and Supplementary Fig. 9b). The increase in these parameters is concomitant with the onset of the light-induced strain in the perovskite films indicated by the red line at 10 minutes in Fig. 5b. We also emphasize that the sudden increase in the carrier mobility described in Fig. 4c also occurs at the same time point of 10 mins. These correlated structure, transport and device data clearly imply that the drastic improvement in the device performance is driven predominantly by the reduction of the effective interlayer distance resulting in the increase in carrier mobility especially along the stacking direction (Fig. 3b).

## Solar Cell Performance

Finally, to test the impact of light-induced contraction on 2D perovskite solar cells fabricated using the three types of crystal structures (DJ  $n=4$ , ACI  $n=3$ , and RP  $n=4$ ), we monitored the evolution of their current-voltage characteristics as a function of illumination time (Fig. 5d). After 10 minutes, we observed significant increase in the  $V_{OC}$  and FF of the DJ and ACI devices, whereas the RP 2D perovskite based solar cells remained almost unchanged as illustrated in Fig. 5e. The overall power conversion efficiency increased by 2.7% in DJ, 3.5% in ACI, and less than 1% in RP based solar cells. The overall increase in the PCE of DJ and ACI 2D perovskite solar cells arises from a combined increase in the  $V_{OC}$  and FF. We do not observe any appreciable change in the  $J_{SC}$  over time, which is consistent with the invariant absorbance spectra measured as a function of light soaking. These improvements in the  $V_{OC}$  and FF are in good agreement with both the correlated in-situ solar cell and x-ray measurements described in Fig. 5a-c and the transport measurements demonstrated in Fig. 4. Moreover, solar cell measurements on DJ, ACI and RP based 2D perovskites are consistent with the fact that light-activated contraction is observed in DJ and ACI, but not in RP 2D perovskites as described in Fig. 2. In addition, to verify the recovery for light-induced interlayer contraction, we performed a cycle of light on and off measurements (Supplementary Fig. 10b). In agreement with the DJ powder and single crystal results, we observed a decrease to the original solar cell efficiency after 23 mins of resting the device in dark. The largest increase for the champion DJ device resulted in the increase in the PCE from 15.6% to 18.3%.

As shown in Fig. 5d and 5e, there are two major changes in the solar cell figures of merit after light-induced contraction, the increase of the fill factor and of the open-circuit voltage. To understand these results, we used our device drift-diffusion model, which calculated the change in the potential barriers height in the bulk by fitting the current-voltage curves before and after light soaking.<sup>20</sup> The simulated current-voltage characteristics before and after 10 minutes of illumination match very the experimental ones. Our simulations indicate that the increase in FF is due to decrease in the potential barrier heights (Supplementary Fig. 10). As shown in our previous work, the FF in 2D perovskite devices is partly governed by the recombination of the photo-generated carriers, which depends on the energy landscape of the stacked 2D quantum-wells.<sup>20</sup> Our results indicate that the light-induced out-of-plane lattice contraction, which results from the enhanced I-I bonding across the interlayers in DJ and ACI perovskite thin films lowers the depth

of the potential barriers, decreasing the number of trapped carriers and thereby reducing the recombination rate. Simulations show that the change in barrier depth for DJ  $n=4$  is  $-26.5$  meV and in ACI  $n=3$  is  $-44.5$ meV. (Supplementary Table 9, 10). Furthermore, the modeling results indicate a 3-fold increase in mobility after light illumination, which is in good agreement with the experimental data from the mobility measurements as illustrated in Fig. 4c.

In addition, device modeling indicates that the light-induced contraction due to enhanced antibonding interaction modifies the ionization energy (valence band to vacuum). This leads to modification of the conduction and valence band energy profiles as validated by the blue shift of the XPS spectra on DJ perovskite films (Supplementary Fig. 6).<sup>30</sup> The change in the EA improves the band alignment between the electron transport layer and the 2D perovskite, thus reducing the amount of energy lost while transporting between the layers. The electron affinity of the 2D perovskite increases from 3.72 eV to 3.81 eV for DJ  $n=4$  and ACI  $n=3$  devices and (Supplementary Table 10) thereby resulting in an increase in the  $V_{OC}$  of the solar cell. We do not observe an increase in the  $J_{SC}$  as the drift-field ( $V=0$  volt) is sufficiently strong to extract the photo-generated carriers, therefore the modification of the energy landscape does not change the short-circuit current.

## Conclusion

In summary, these results have two key implications. First, they demonstrate that by selecting the appropriate interlayer cations and by leveraging the acute sensitivity of 2D hybrid perovskites to external stimuli, the band-gap discontinuity in the out-of-plane direction can be surmounted and charge transport properties on-par with the 3D perovskites can be realized. Second, these results pave the path for understanding and tailoring novel light-matter interactions, similar to those explored in 2D transition metal dichalcogenides, which arises when excitations are coupled across the layered perovskite layers separated by short organic cations.

**Acknowledgments:** The work at Rice University was supported by the DoD-STIR program funded by ARO. J.E. acknowledges the financial support from the Institut Universitaire de France. W.L. acknowledge NSF GRFP. This material is based upon work supported by the National Science Foundation Graduate Research Fellowship Program under Grant No. (NSF 20-587). Any opinions, findings, and conclusions or recommendations expressed in this material are those of the author and do not necessarily reflect the views of the National Science Foundation. Work at Northwestern on the stability of perovskite solar cells was supported by the ONR (N00014-20-1-2725). DFT calculations were performed at Institut FOTON as well as ISCR and the work was granted access to the HPC resources of TGCC/CINES/IDRIS under the allocations 2019-A0060906724 and 2019-A0070907682 made by GENCI. This research used facilities of the Advanced Photon Source, a U.S Department of Energy (DOE) Office of Science User Facility operated for the DOE Office of Science by Argonne National Laboratory under Contrast No. DE-AC02-06CH11357. This research used beamline 11BM (CMS) of the National Synchrotron Light Source II and the Center for Functional Nanomaterials (CFN), both of which are U.S. Department of Energy (DOE) Office of Science User Facilities operated for the DOE Office of Science by Brookhaven National Laboratory under Contract No. DE-SC0012704. We acknowledge the help of Bo Chen for supervising the XPS measurements. We thank Ruipeng Li for his assistance performing experiments at beamline CMS. The work at Purdue University was supported by the National Science Foundation under Grant No. #1724728, CIF21 DIBBs: EI: Creating a Digital Environment for Enabling Data-Driven Science (DEEDS), awarded by the Office of Advanced Cyberinfrastructure (OAC).

**Author contributions:** A. D. M and J.C.B conceived the concept, designed the experiment, and wrote the manuscript. S.S. and J. Hoffman. synthesized the perovskite crystals and prepared the samples with the help of J. Hou. and W.L., and under the supervision of M.G.K.. S.S. fabricated thin films and the solar cells and performed solar cell characterization. W.L. measured and analyzed the GIWAXS patterns with the help of H.Z., Y.W, A.F., J. Essman, J.S., E.T. and performed indexing with guidance from J. Even and J.-C.B.. DFT calculations were performed by B.T. with guidance from J. Even and C. K.. Device modelling was done by R.A. advised by M.A.A.. J.J.C helped with the data analysis. All authors read the manuscript and agree to its contents, and all data are reported in the main text and supplemental materials.

**Competing interests:** The authors declare no competing interests.

**Figure Legend:**

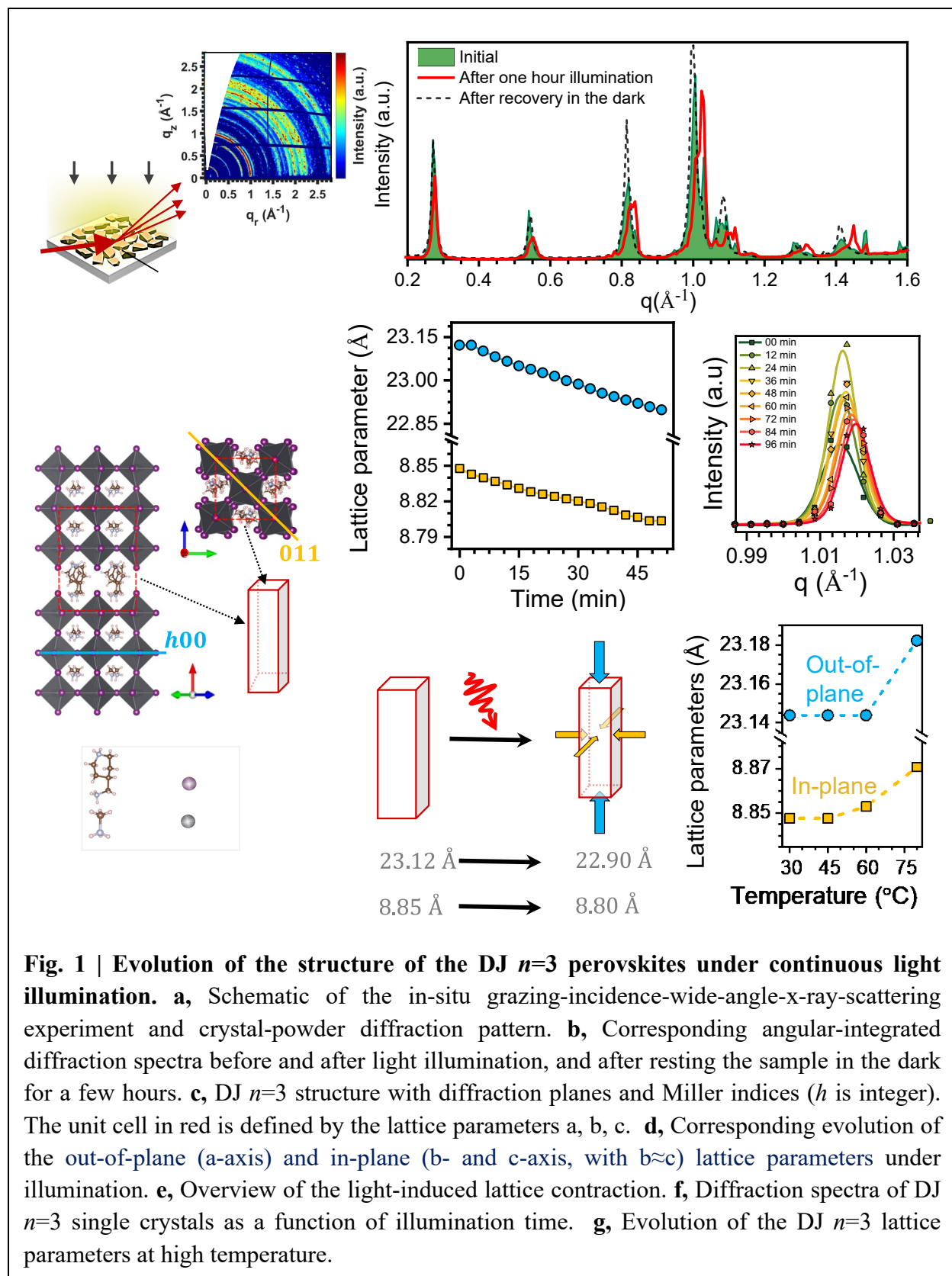
Figure 1: Evolution of the structure of the DJ  $n=3$  perovskites under continuous light illumination.

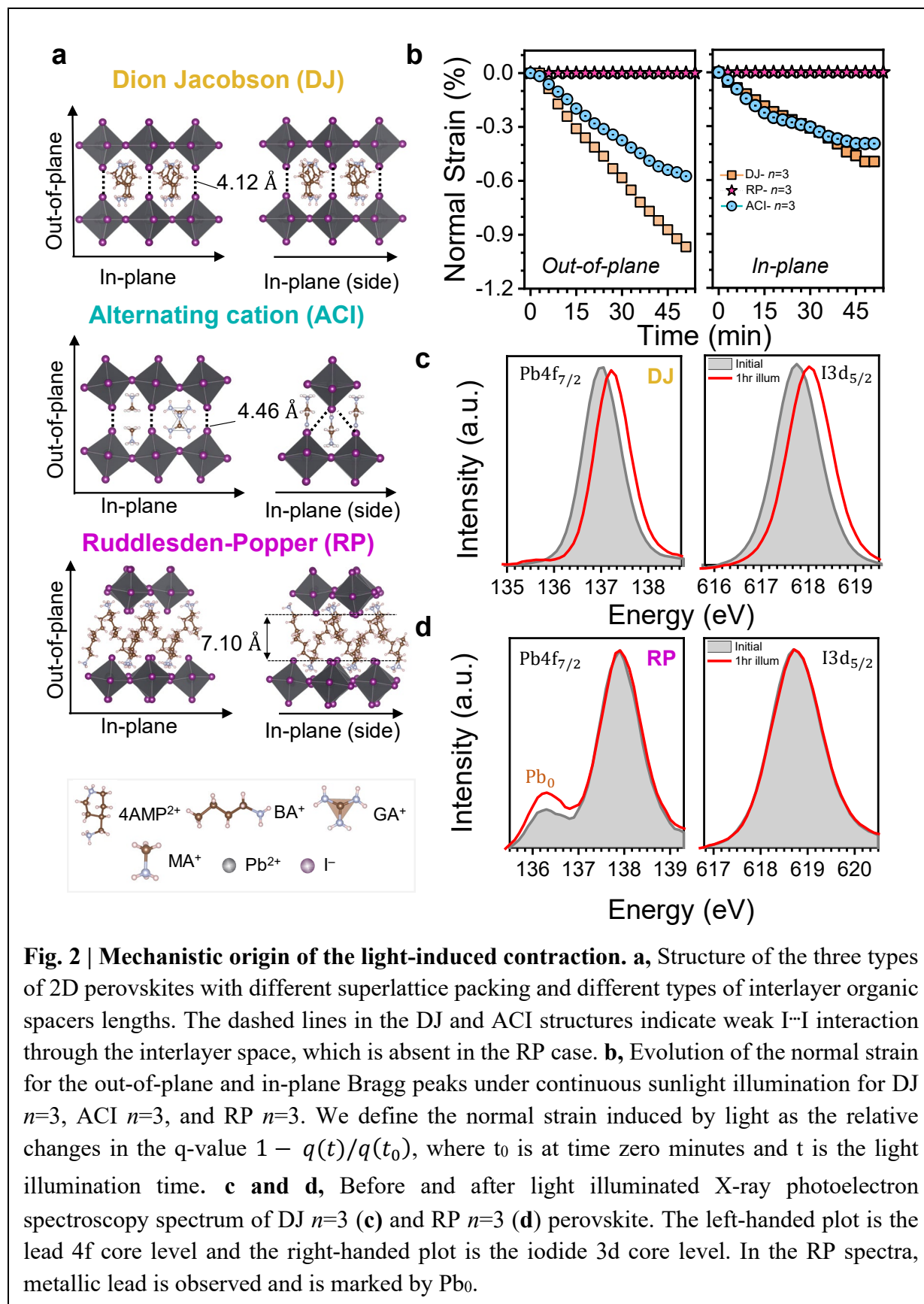
Figure 2: Mechanistic origin of the light-induced contraction.

Figure 3: Light-activated interlayer contraction.

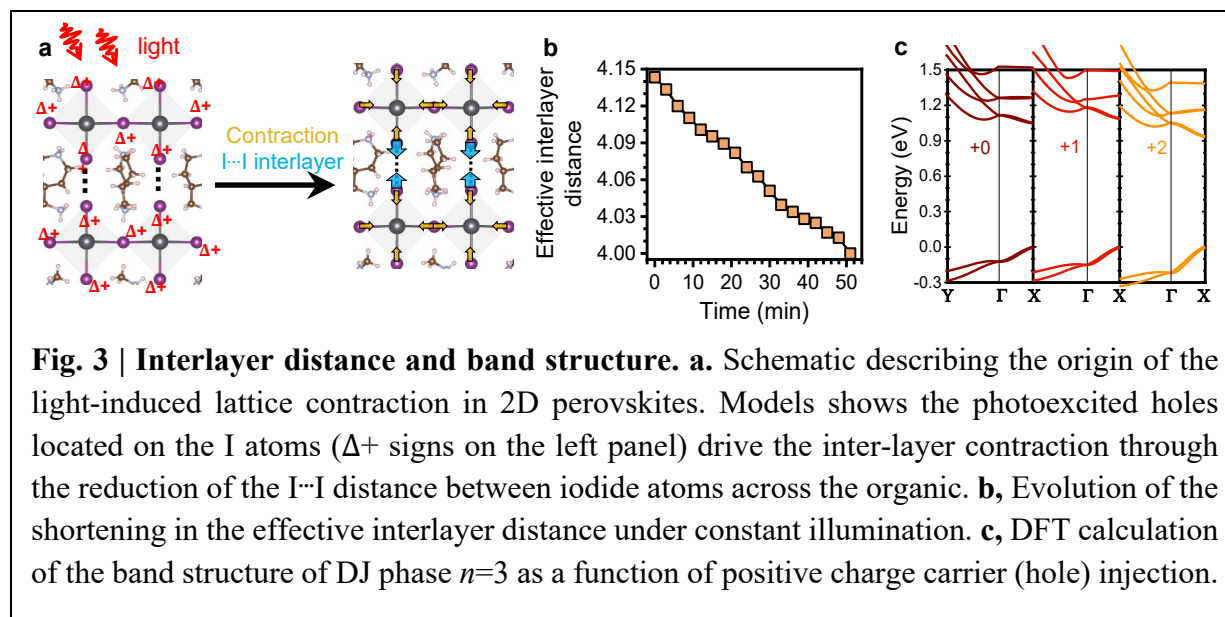
Figure 4: Changes in the electron mobility as a function of light illumination.

Figure 5: Effects of continuous light illumination on the performances of 2D perovskite solar cells





**Fig. 2 | Mechanistic origin of the light-induced contraction.** **a**, Structure of the three types of 2D perovskites with different superlattice packing and different types of interlayer organic spacers lengths. The dashed lines in the DJ and ACI structures indicate weak I<sup>-</sup>I interaction through the interlayer space, which is absent in the RP case. **b**, Evolution of the normal strain for the out-of-plane and in-plane Bragg peaks under continuous sunlight illumination for DJ  $n=3$ , ACI  $n=3$ , and RP  $n=3$ . We define the normal strain induced by light as the relative changes in the  $q$ -value  $1 - q(t)/q(t_0)$ , where  $t_0$  is at time zero minutes and  $t$  is the light illumination time. **c** and **d**, Before and after light illuminated X-ray photoelectron spectroscopy spectrum of DJ  $n=3$  (**c**) and RP  $n=3$  (**d**) perovskite. The left-handed plot is the lead 4f core level and the right-handed plot is the iodide 3d core level. In the RP spectra, metallic lead is observed and is marked by Pb<sub>0</sub>.



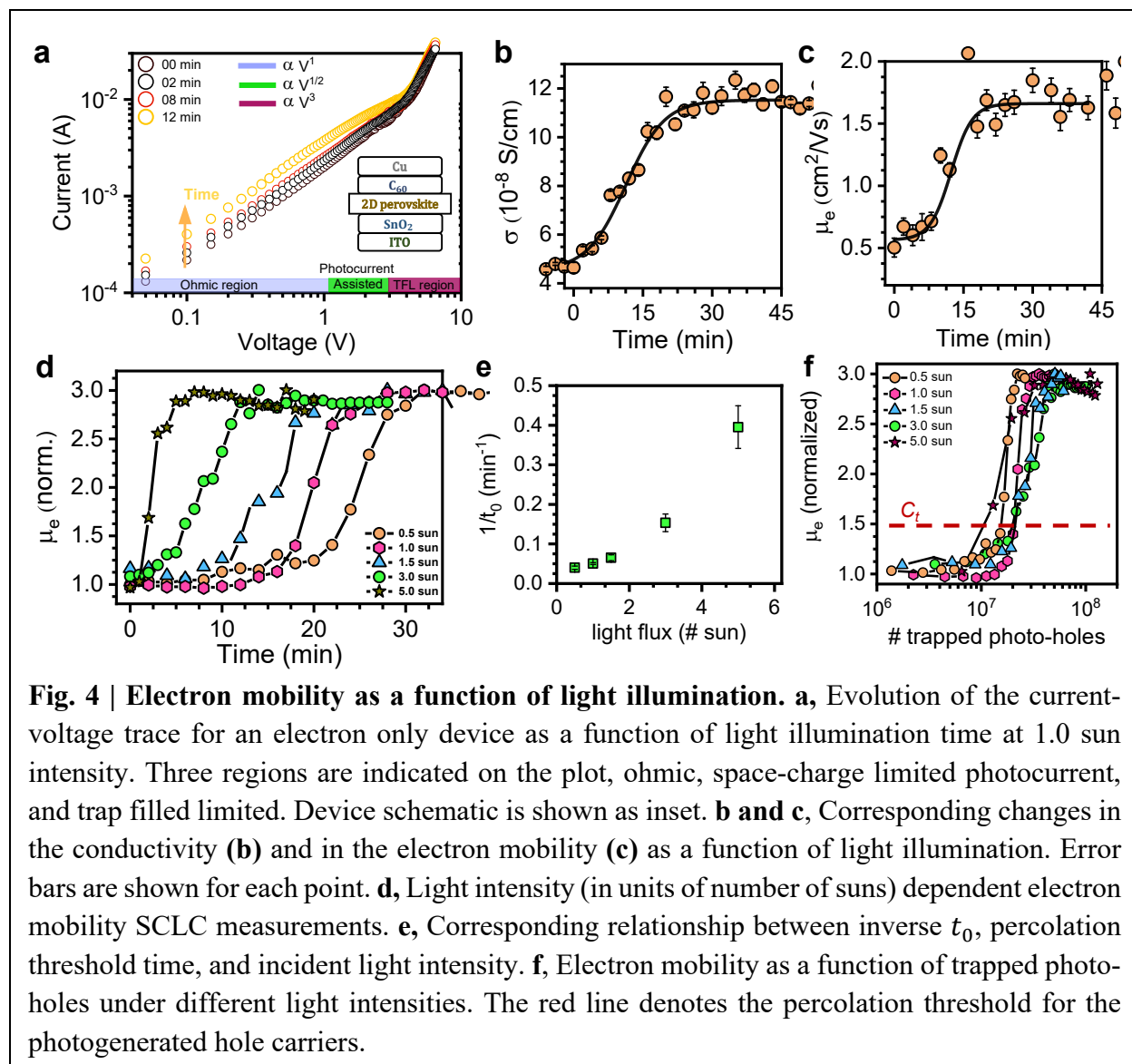


**Fig. 4 | Electron mobility as a function of light illumination.** **a**, Evolution of the current-voltage trace for an electron only device as a function of light illumination time at 1.0 sun intensity. Three regions are indicated on the plot, ohmic, space-charge limited photocurrent, and trap filled limited. Device schematic is shown as inset. **b and c**, Corresponding changes in the conductivity (**b**) and in the electron mobility (**c**) as a function of light illumination. Error bars are shown for each point. **d**, Light intensity (in units of number of suns) dependent electron mobility SCLC measurements. **e**, Corresponding relationship between inverse  $t_0$ , percolation threshold time, and incident light intensity. **f**, Electron mobility as a function of trapped photo-holes under different light intensities. The red line denotes the percolation threshold for the photogenerated hole carriers.

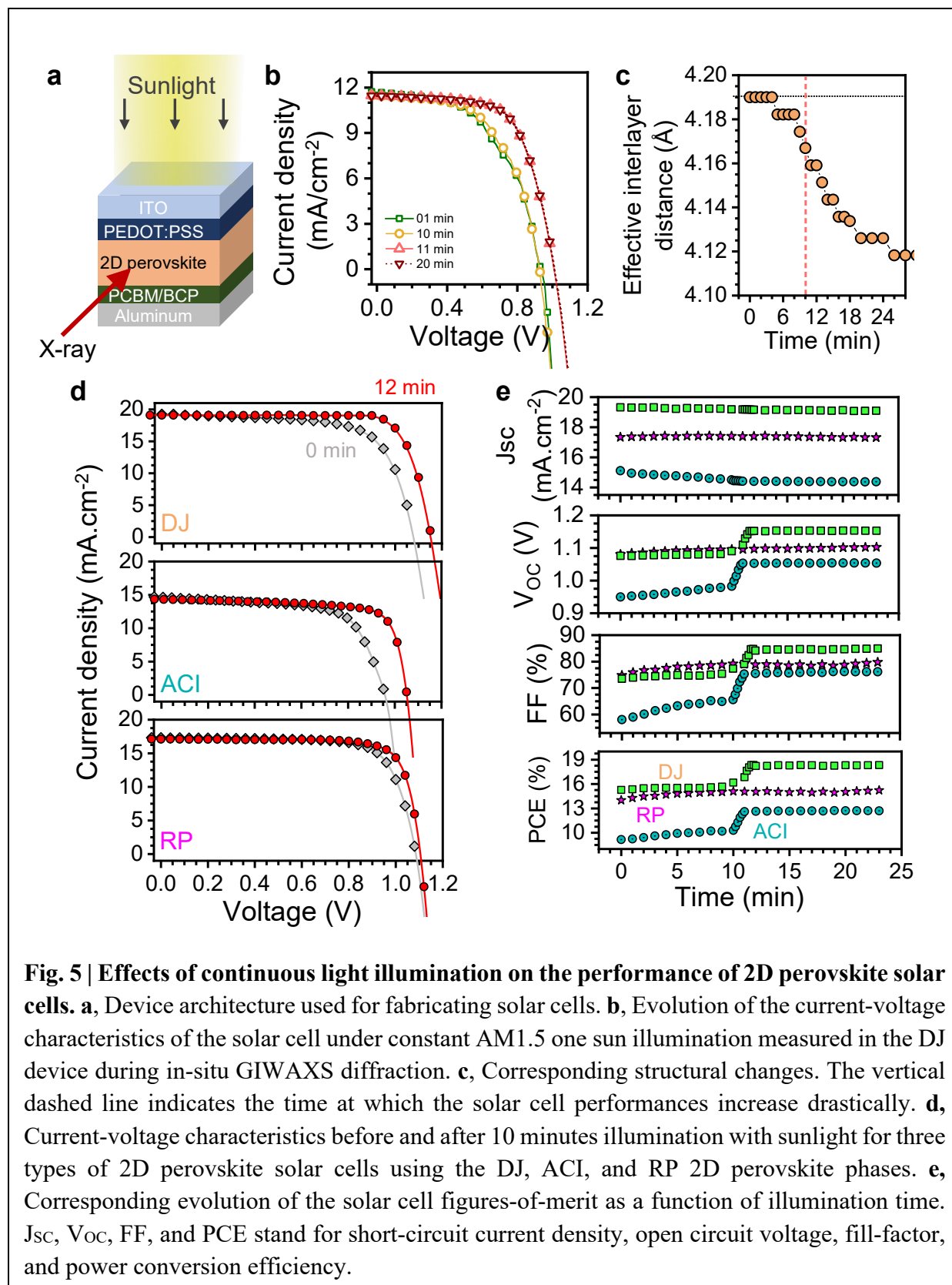


**Fig. 5 | Effects of continuous light illumination on the performance of 2D perovskite solar cells.** **a**, Device architecture used for fabricating solar cells. **b**, Evolution of the current-voltage characteristics of the solar cell under constant AM1.5 one sun illumination measured in the DJ device during in-situ GIWAXS diffraction. **c**, Corresponding structural changes. The vertical dashed line indicates the time at which the solar cell performances increase drastically. **d**, Current-voltage characteristics before and after 10 minutes illumination with sunlight for three types of 2D perovskite solar cells using the DJ, ACI, and RP 2D perovskite phases. **e**, Corresponding evolution of the solar cell figures-of-merit as a function of illumination time. J<sub>sc</sub>, V<sub>oc</sub>, FF, and PCE stand for short-circuit current density, open circuit voltage, fill-factor, and power conversion efficiency.

## References

1. Mitzi, D. B., Chondroudis, K. & Kagan, C. R. Organic-inorganic electronics. *IBM J. Res. Dev.* **45**, 29–45 (2001).
2. Tsai, H. *et al.* High-efficiency two-dimensional Ruddlesden–Popper perovskite solar cells. *Nature* **536**, 312–316 (2016).
3. Yuan, M. *et al.* Perovskite energy funnels for efficient light-emitting diodes. *Nat. Nanotechnol.* **11**, 872–877 (2016).
4. Long, G. *et al.* Spin control in reduced-dimensional chiral perovskites. *Nat. Photonics* **12**, 528–533 (2018).
5. Lu, H. *et al.* Spin-dependent charge transport through 2D chiral hybrid lead-iodide perovskites. *Sci. Adv.* **5**, eaay0571 (2019).
6. Chen, Y. *et al.* 2D Ruddlesden–Popper Perovskites for Optoelectronics. *Adv. Mater.* **30**, 1703487 (2018).
7. Cao, D. H., Stoumpos, C. C., Farha, O. K., Hupp, J. T. & Kanatzidis, M. G. 2D Homologous Perovskites as Light-Absorbing Materials for Solar Cell Applications. *J. Am. Chem. Soc.* **137**, 7843–7850 (2015).
8. Mao, L., Stoumpos, C. C. & Kanatzidis, M. G. Two-Dimensional Hybrid Halide Perovskites: Principles and Promises. *J. Am. Chem. Soc.* **141**, 1171–1190 (2019).
9. Billing, D. G. & Lemmerer, A. Synthesis, characterization and phase transitions of the inorganic–organic layered perovskite-type hybrids [(C<sub>n</sub>H<sub>2n+1</sub>NH<sub>3</sub>)<sub>2</sub>PbI<sub>4</sub>] (n = 12, 14, 16 and 18). *New J. Chem.* **32**, 1736–1746 (2008).
10. Billing, D. G. & Lemmerer, A. Synthesis and crystal structures of inorganic–organic hybrids incorporating an aromatic amine with a chiral functional group. *CrystEngComm* **8**, 686–695 (2006).
11. Mitzi, D. B. Synthesis, Structure, and Properties of Organic-Inorganic Perovskites and Related Materials. in *Progress in Inorganic Chemistry* 1–121 (John Wiley & Sons, Ltd, 1999). doi:10.1002/9780470166499.ch1.
12. Tu, Q. *et al.* Out-of-Plane Mechanical Properties of 2D Hybrid Organic–Inorganic Perovskites by Nanoindentation. *ACS Appl. Mater. Interfaces* **10**, 22167–22173 (2018).
13. Reyes-Martinez, M. A. *et al.* Unraveling the Elastic Properties of (Quasi)Two-Dimensional Hybrid Perovskites: A Joint Experimental and Theoretical Study. *ACS Appl. Mater. Interfaces* **12**, 17881–17892 (2020).
14. Katan, C., Mercier, N. & Even, J. Quantum and Dielectric Confinement Effects in Lower-Dimensional Hybrid Perovskite Semiconductors. *Chem. Rev.* **119**, 3140–3192 (2019).
15. Spanopoulos, I. *et al.* Uniaxial Expansion of the 2D Ruddlesden–Popper Perovskite Family for Improved Environmental Stability. *J. Am. Chem. Soc.* **141**, 5518–5534 (2019).
16. Gompel, W. T. M. V. *et al.* Towards 2D layered hybrid perovskites with enhanced functionality: introducing charge-transfer complexes via self-assembly. *Chem. Commun.* **55**, 2481–2484 (2019).

17. Ahn, J. *et al.* A new class of chiral semiconductors: chiral-organic-molecule-incorporating organic–inorganic hybrid perovskites. *Mater. Horiz.* **4**, 851–856 (2017).
18. Mao, L. *et al.* Hybrid Dion–Jacobson 2D Lead Iodide Perovskites. *J. Am. Chem. Soc.* **140**, 3775–3783 (2018).
19. Soe, C. M. M. *et al.* New Type of 2D Perovskites with Alternating Cations in the Interlayer Space,  $(\text{C}(\text{NH}_2)_3)(\text{CH}_3\text{NH}_3)_n\text{PbI}_{3n+1}$ : Structure, Properties, and Photovoltaic Performance. *J. Am. Chem. Soc.* **139**, 16297–16309 (2017).
20. Tsai, H. *et al.* Design principles for electronic charge transport in solution-processed vertically stacked 2D perovskite quantum wells. *Nat. Commun.* **9**, 2130 (2018).
21. Zhang, Y., Sun, M., Zhou, N., Huang, B. & Zhou, H. Electronic Tunability and Mobility Anisotropy of Quasi-2D Perovskite Single Crystals with Varied Spacer Cations. *J. Phys. Chem. Lett.* **11**, 7610–7616 (2020).
22. Soe, C. M. M. *et al.* Structural and thermodynamic limits of layer thickness in 2D halide perovskites. *Proc. Natl. Acad. Sci.* **116**, 58–66 (2019).
23. Leng, K. *et al.* Molecularly thin two-dimensional hybrid perovskites with tunable optoelectronic properties due to reversible surface relaxation. *Nat. Mater.* **17**, 908–914 (2018).
24. Liu, G. *et al.* Isothermal pressure-derived metastable states in 2D hybrid perovskites showing enduring bandgap narrowing. *Proc. Natl. Acad. Sci.* **115**, 8076–8081 (2018).
25. Liu, S. *et al.* Manipulating efficient light emission in two-dimensional perovskite crystals by pressure-induced anisotropic deformation. *Sci. Adv.* **5**, eaav9445 (2019).
26. Yu, S. *et al.* Nonconfinement Structure Revealed in Dion–Jacobson Type Quasi-2D Perovskite Expedites Interlayer Charge Transport. *Small* **15**, 1905081 (2019).
27. Blancon, J.-C., Even, J., Stoumpos, C. C., Kanatzidis, M. G. & Mohite, A. D. Semiconductor physics of organic–inorganic 2D halide perovskites. *Nat. Nanotechnol.* **15**, 969–985 (2020).
28. Giovanni, D. *et al.* The Physics of Interlayer Exciton Delocalization in Ruddlesden–Popper Lead Halide Perovskites. *Nano Lett.* **21**, 405–413 (2021).
29. Santomauro, F. G. *et al.* Localized holes and delocalized electrons in photoexcited inorganic perovskites: Watching each atomic actor by picosecond X-ray absorption spectroscopy. *Struct. Dyn.* **4**, 044002 (2016).
30. Zu, F.-S. *et al.* Impact of White Light Illumination on the Electronic and Chemical Structures of Mixed Halide and Single Crystal Perovskites. *Adv. Opt. Mater.* **5**, 1700139 (2017).
31. Blancon, J.-C. *et al.* Extremely efficient internal exciton dissociation through edge states in layered 2D perovskites. *Science* **355**, 1288–1292 (2017).
32. Zhang, Z., Fang, W.-H., Tokina, M. V., Long, R. & Prezhdo, O. V. Rapid Decoherence Suppresses Charge Recombination in Multi-Layer 2D Halide Perovskites: Time-Domain Ab Initio Analysis. *Nano Lett.* **18**, 2459–2466 (2018).
33. Neutzner, S. *et al.* Exciton-polaron spectral structures in two-dimensional hybrid lead-halide perovskites. *Phys. Rev. Mater.* **2**, 064605 (2018).
34. Ren, H. *et al.* Efficient and stable Ruddlesden–Popper perovskite solar cell with tailored interlayer molecular interaction. *Nat. Photonics* **14**, 154–163 (2020).

35. Shi, D. *et al.* Low trap-state density and long carrier diffusion in organolead trihalide perovskite single crystals. *Science* **347**, 519–522 (2015).
36. Goodman, A. M. & Rose, A. Double Extraction of Uniformly Generated Electron-Hole Pairs from Insulators with Noninjecting Contacts. *J. Appl. Phys.* **42**, 2823–2830 (1971).
37. Mihailetschi, V. D., Wildeman, J. & Blom, P. W. M. Space-Charge Limited Photocurrent. *Phys. Rev. Lett.* **94**, 126602 (2005).
38. Ma, C., Shen, D., Ng, T.-W., Lo, M.-F. & Lee, C.-S. 2D Perovskites with Short Interlayer Distance for High-Performance Solar Cell Application. *Adv. Mater.* **30**, 1800710 (2018).
39. Kirkpatrick, S. Percolation and Conduction. *Rev. Mod. Phys.* **45**, 574–588 (1973).
40. Seager, C. H. & Pike, G. E. Percolation and conductivity: A computer study. II. *Phys. Rev. B* **10**, 1435–1446 (1974).

## Methods

**Materials.** 2D perovskite precursors such as methylamine hydrochloride (MAI), lead oxide (PbI<sub>2</sub>), butylamine (BA), 4-aminomethyl piperidine (4AMP), guanidinium hydrochloride (GACl), anhydrous dimethyl formamide (DMF), dimethyl sulfoxide (DMSO), and hydroiodic (HI) were purchased from Sigma Aldrich. Methylamine iodide (MAI) was purchased from Greatcell Solar. For device fabrication: indium tin oxide (ITO) is from Thin Film Device Inc, Phenyl-C61-butyric acid methyl ester (PCBM) is from Sigma Aldrich, poly(3,4-ethylenedioxythiophene) polystyrene sulfonate (PEDOT:PSS) is from Heraeus Epurio.

### Crystal and thin films fabrication

*Powder crystal synthesis:* As previously reported in ref 1 and 2, the 2D Ruddlesden-Popper (RP) perovskite crystals of BA<sub>2</sub>MA<sub>2</sub>Pb<sub>3</sub>I<sub>10</sub> were synthesized by mixing lead oxide (PbO, 99%), methylamine hydrochloride (MAI, ≥98%) and butylamine (BA, 99.5%) in appropriate ratios in a mixture of hydroiodic acid (HI, 57 wt% in H<sub>2</sub>O) and hypophosphorous acid (H<sub>3</sub>PO<sub>2</sub>, 50% in H<sub>2</sub>O). Further, The solution was stirred at 190°C until all the precursors were dissolved, then allowed to cool down to room temperature. This resulted in the crystallization of platelet-like powders with micrometer to millimeter in size. The Dion-Jacobson (DJ) perovskite crystals of (4AMP)-MA<sub>2</sub>Pb<sub>3</sub>I<sub>10</sub> were prepared by combining PbO, MAI, and 4-aminomethyl piperidine (4AMP, 96%) in appropriate ratios in a HI/H<sub>3</sub>PO<sub>2</sub> solvent mixture. The solution was stirred at 240°C until all the precursors were dissolved, then allowed to cool down to room temperature. This resulted in the crystallization of platelet-like powders with micrometer to millimeter in size. A detailed synthesis procedure is reported in ref 3. The Alternating Cation (ACI) perovskite crystals of (GA)MA<sub>3</sub>Pb<sub>3</sub>I<sub>10</sub> were prepared by combining PbO, MAI, and guanidinium hydrochloride (GACl, 99%) in appropriate ratios in a HI/H<sub>3</sub>PO<sub>2</sub> solvent mixture. The solution was stirred at 190°C until all the precursors were dissolved, then allowed to cool down to room temperature. This resulted in the crystallization of platelet-like powders with micrometer to millimeter in size. A detailed synthesis procedure is reported in ref 4. Finally, batches of synthesized 2D perovskite crystals were characterized using one-dimensional X-ray diffraction (XRD: Rigaku D/Max Ultima II) to determine their initial phase purity and crystal quality. Different *n* value thicknesses of the 2D perovskites were obtained by altering the stoichiometry of the reactants in the RP, DJ, and ACI perovskites as reported in ref 1,3, and 4

*Film fabrication:* To produce 2D perovskite thin films for solar cell devices, we first dissolved the synthesized parent-crystal powders in a solvent with different additives. The  $\text{BA}_2\text{MA}_3\text{Pb}_4\text{I}_{13}$  and  $(\text{GA})\text{MA}_3\text{Pb}_3\text{I}_{10}$  solution was obtained by dissolving 0.4 g of the parent crystals and 0.02 g of dried MAI in 1 ml of anhydrous DMF. The  $(4\text{AMP})\text{-MA}_3\text{Pb}_4\text{I}_{13}$  solution was prepared by dissolving 0.4 g of parent-crystals in 1 ml of anhydrous DMF/DMSO (1:1) with 1  $\mu\text{l}$  of HI. The prepared solution was left on the hotplate at 70°C for 6 hours. After cooling down, 100  $\mu\text{l}$  of the prepared solution was instantly dropped and spin coated over substrates at 4000 rpm for 30 seconds followed by annealing at 100°C for 10 minutes, resulting in the formation of the 2D perovskite thin films.

*Large area single crystal synthesis:* The Dion-Jacobson ( $n=3$ )  $(4\text{AMP})(\text{MA})_2\text{Pb}_3\text{I}_{10}$  single crystal was synthesized using PbO (Sigma-Aldrich, >99%), 4-AMP (>96%), and MAI (>99.9%), HI acid (57.0 wt % in  $\text{H}_2\text{O}$ ), and  $\text{H}_3\text{PO}_2$  acid solution (50% w.t. in  $\text{H}_2\text{O}$ ). The PbO, 4-AMP, and MAI were mixed with the appropriate ratio in a HI/  $\text{H}_3\text{PO}_2$  solution indicated in ref 3 and stirred at 240°C until dissolved. The solution was then diluted with 3 times the amount of HI. Afterward, a 10  $\mu\text{L}$  of the diluted solution was dropped onto the glass surface and sandwiched by another piece of glass. This system was then annealed for 8 hours at 60 °C resulting in large millimeter sized perovskite single crystal. Further details can be found in ref 5. The glass substrates used in this procedure were washed in water, acetone, acetone/ethanol (50:50) and isopropyl alcohol by ultrasonication for 15 min, respectively.

### **Solar cell devices fabrication**

We used an inverted planar device architecture with indium tin oxide (ITO)/hole transport layer (HTL)/2D perovskite-film/electron transport layer (ETL)/Aluminum (Al), for the solar cells as depicted in Fig. 3. This solar cell architecture used PEDOT:PSS (Clevios™ PEDOT:PSS) as the HTL and [6,6]-phenyl- $\text{C}_{61}$ -butyric acid methyl ester (PCBM, Sigma Aldrich, 99.9%) as the ETL. Film fabrication steps are shown below. We first washed the patterned ITO in water, acetone, acetone/ethanol (50:50) and isopropyl alcohol by ultrasonication for 15 min, respectively. The substrate was further dried under argon airflow and treated with UV for 30 min. A PEDOT:PSS layer was spin-coated on the clean ITO substrate at 5000 rpm for 30 seconds followed by annealing at 150°C for 30 min to obtain a layer thickness of about 30 nm. The ITO/PEDOT:PSS substrates

were subsequently transferred to an argon-filled glovebox. Using the methodology from the film fabrication section in above section, we fabricated 2D perovskite thin films of approximately 250nm thickness on top of the ITO/PEDOT:PSS substrate. To prepare the ETL, we dissolved 25mg of PCBM in 1ml of chlorobenzene and stirred overnight at 60°C. Afterward, a 50 $\mu$ l of the PCBM solution was dropped on the ITO/PEDOT:PSS/2D perovskite sample and spin-coated at 1000 rpm for 45 seconds to form a 30nm ETL thin film. The solar cell device was completed by evaporating a 100 nm layer of aluminum using a shadow mask, yielding eight cells of 31.4 mm<sup>2</sup> per 1'x1' area of the sample device.

### **Solar cell devices characterization**

The performances of the fabricated solar cells were characterized by measuring the current-voltage (J-V) curves of each device illuminated by an ABB solar simulator from Newport (model 94011). The arc simulator modeled AM 1.5G irradiance of 100 mW/cm<sup>2</sup> and was calibrated using a NIST-certified Si solar cell (Newport 91150V, ISO 17025). The current was measured with a Keithley 2401 instrument at different voltage scan rate.

### **Grazing incidence wide angle X-ray scattering (GIWAXS)**

*In-Situ GIWAXS measurements:* All diffraction spectra used in this paper were high-resolution synchrotron GIWAXS patterns measured at two beamlines: 8-ID-E at the Advanced Photon Source (APS) and 11-BM at the National Synchrotron Light Source-II (NSLS II). At beamline 8-ID-E, samples were placed on a Linkam grazing incidence x-ray-scattering (GIXS) stage (temperature controlled at 25°C) inside a vacuum chamber (10<sup>-4</sup> torr) with the sample 228 mm away from a Pilatus 1M (Dectris) area detector. The photon energy was 10.91 keV, and the beam size was 200  $\mu$ m x 20  $\mu$ m (H x V). At beamline 11-BM, two different staging schematics were used for GIWAXS measurements: (a) an in-lab-built GIXS chamber (which circulated High Purity Helium gas) with the sample 257 mm away from a Pilatus 300M (Dectris) area detector and (b) robotic stage inside a vacuum chamber (10<sup>-2</sup> torr) with the sample 267mm away from a Pilatus 800K (Dectris) area detector. The photon energy was 13.5 keV, and the beam size was 200  $\mu$ m x 50  $\mu$ m (H x V).

For the in-situ light illuminated crystal GIWAXS measurements, we installed a Newport Class ABB solar simulator on top of each beamline chambers (schematic (a) staging chamber for

beamline 11-BM) and illuminating with 1-Sun (AM 1.5G) irradiance. To calibrate the solar simulator illumination irradiance for all in-situ GIWAXS measurements, we measured  $100\text{mW}/\text{cm}^2$  using a NIST-certified Si solar cell (Newport 91150V, ISO 17025). After each powder light illumination experiment, samples were directly transferred to a vacuum chamber ( $10^{-2}$  to  $10^{-4}$  torr) for relaxation. All in-situ light illumination GIWAXS patterns were acquired at 3-minute intervals, an X-ray incident angle of  $0.15^\circ$ , and a 3-second exposure time. For the in-situ light illuminated device measurements, we used the same exact setup as for the GIWAXS measurements of crystals but connected a Keithley 2400 multimeter to the device through a feedthrough. The GIWAXS patterns and current-voltage responses were acquired at every 1-2 minutes intervals, at an X-ray incident angle of  $0.24^\circ$ , and a 5 second exposure time.

Temperature dependent GIWAXS measurements were obtained at both the APS and NSLS-II beamline. At the APS beamline, temperature dependent measurements were obtained by cooling to liquid nitrogen temperatures and heating up to  $80^\circ\text{C}$  using the Linkam GIXS stage. An incident angle of  $0.15^\circ$  and a 5 second exposure time were used at both beamlines for the temperature measurements.

Three types of samples were used for the in-situ light illumination measurement: synthesized powder crystals, millimeter sized single crystal and thin-film devices. Powder crystals were used for the temperature dependent measurements. Samples were all sealed in an airtight vacuum bag purged with Argon right up until the measurements. Powder GIWAXS measurement were performed by crushing and smearing the powder crystal onto clean glass substrates (wiped with Acetone and Isopropyl alcohol using Kim wipes).

*GIWAXS data processing:* GIWAXS data from the APS beamline were processed using the GIXSGUI package (version 1.7.3) running on Matlab 2018b (Mathworks).<sup>7</sup> GIWAXS data from the NSLS-II beamline were processed using SciAnalysis (<https://github.com/CFN-softbio/SciAnalysis>) running on Visual Studio Code using Python (version 3.7.3).<sup>8</sup> All patterns were corrected with conditions such as detector sensitivity, X-ray polarization, and geometrical solid-angle parameters.

*GIWAXS analysis:* To analyze the in-situ light illuminated GIWAXS measurements, numerical fitting of the diffraction profiles was performed in Matlab 2018b. Each diffraction peak range was fitted with pseudo-Voigt profiles.<sup>6</sup> Each fit used the built-in “fmincon” function which constrained the pseudo-Voigt profile to physical ranges in terms of peak linewidth (full-width-at-half-maximum FWHM). This allowed the fit to discard unphysical domain boundaries/crystallite size. Due to the small residual from the “fmincon” fit, the error interval is smaller than the size of each point in the strain and lattice parameter plot.

The Debye-Scherrer formula was used to extract the average grain size of the 2D perovskites.<sup>9</sup> The first order out-of-plane diffraction plane was used for the analysis. The shape factor of 0.9 (K value in the Scherrer equation) was used.<sup>9</sup> The Scherrer formula is:

$$D_{hkl} = \frac{K\lambda}{\beta_{hkl} \cos(\theta_{hkl})}$$

where,  $\theta_{hkl}$  is the Bragg scattering angle and  $\beta_{hkl}$  is the full-width-at-half-max (FWHM). Since this is a grazing scattering geometry with area detectors, we have corrected the FWHM for the beam divergence ( $\beta_{div}$ ) and the energy bandwidth ( $\beta_{BW}$ ).<sup>10</sup> The geometric smearing is neglected for small Bragg scattering angles. The FWHM correction is given by:

$$\beta_{hkl} = \sqrt{\beta_{experiment}^2 - \beta_{res}^2}$$

$$\beta_{res} = \sqrt{\beta_{div}^2 + \beta_{BW}^2}$$

*Effective interlayer distance calculations:* Due to the uniform stacking of the Dion-Jacobson perovskite, the out-of-plane and in-plane diffraction axis are deconvoluted. With this and the assumption that perovskite octahedra does not undergo a large distortion (confirm by DFT calculations) we formulate the effective interlayer distance as the following:

$$\text{Effective interlayer distance } (t) = D_{300}(t) - 3 * D_{011}(t)$$

Where  $t$  is the light illumination time,  $D_{300}$  is the out-of-plane d-spacing and the  $D_{011}$  is the in-plane d-spacing.

### **X-ray photo-electron spectroscopy**

X-ray photoelectron spectroscopy measurements were carried out on a PHI Quantera XPS system. Before and after light illumination XPS was performed on a large millimeter size Dion-Jacobson

and Ruddlesden Popper  $n=3$  single crystal perovskite and film grown on a glass substrate using the procedure mentioned in section 1. Etching was not performed, and the sample environment was under  $10^{-8}$  torr for the duration of the experiment. Each peak was averaged using 20-25 spectra collected. Emission spectra were calibrated to carbon 1s photoelectron emission at 284.80eV. The samples were illuminated using an ABB solar simulator from Newport (model 94011) for one hours. The XPS spectra were fitted to a pseudovoigt profile, and the error was extract using a the “nlparci” function in MATLAB from the Jacobian of the fit.

### **Transport characterization**

We fabricated an electron-only device with indium tin oxide (ITO)/ tin oxide ( $\text{SnO}_2$ ) on one side and then  $\text{C}_{60}/\text{Cu}$  on the other side. 2D perovskite thin films was measured about 250nm in thickness. The samples were illuminated using an ABB solar simulator from Newport (model 94011) for 40mins. The arc simulator modeled AM 1.5G irradiance of  $100 \text{ mW}/\text{cm}^2$  and was calibrated using a NIST-certified Si solar cell (Newport 91150V, ISO 17025). The current was measured with a Keithley 2401 instrument at scan rate of .5V /s. Device was measured in vacuum ( $10^{-2}$  torr). The analysis was performed by fitting in MATLAB and using the optimization package and a numerical least square algorithm “lsqcurvefit”. An error bar for conductivity and mobility was extracted by using the Jacobian of each time fit. We used the “nlparci” function in MATLAB’s optimization package to extract a 95% confidence interval and the error was the absolute difference of the interval.

### **Theoretical structural simulation**

*Density Functional Theory simulations:* The calculations were performed using Density Functional Theory (DFT)<sup>12,13</sup> as implemented in the SIESTA package with a basis set of finite-range of numerical atomic orbitals.<sup>14</sup> We used the van der Waals density functional with C09 exchange within the van der Waals DF2 flavor to describe the exchange-correlation term.<sup>15,16</sup> This tuning was suggested to improve C09 based geometry optimization over that with DF1 flavor.<sup>16</sup> The latter has already provided a good description of experimental lattice constants similar to those obtained with optimized GGA-based PBEsol functional in solids.<sup>17,18</sup> Norm-conserving Troullier-Martins pseudopotentials were used for each atomic species to account for the core electrons.<sup>19</sup>  $1s^1$ ,  $2s^2 2p^2$ ,  $2s^2 2p^3$ ,  $5s^2 5p^5$  and  $5d^{10} 6s^2 6p^2$ ,  $2s^2 2p^4$  and  $4s^2 3d^8$  were used as valence electrons for H,

C, N, I, Pb, respectively. Polarized Double-Zeta (DZP) basis set with an energy shift of 200 meV were used for the calculations. For the real space mesh grids, an energy cutoff of 600 Rydberg was used. We used the following Monkhorst-Pack k-point grids for the different systems: 2x8x8 for the DJ compound; 4x1x4 and 4x4x1 for the ACI n=2 and n=3, respectively; 6x1x6 for the BA compound. The different structures were fully relaxed using the fast-inertial relaxation engine (FIRE) algorithm and the maximum force was set to 0.05 eV/Å.<sup>20</sup> Since it is not possible in the official distribution of SIESTA to perform structural relaxations while keeping the original symmetries, we constrained the angles of the different structures to 90° ( $\alpha=\beta=\gamma=90^\circ$ ) during the geometry optimization such that they remain in their orthorhombic starting systems. Charges were injected into the system by either adding (electron injection) or removing (hole injection) the desired number of electrons. In doing so, the simulation code applies a compensating background charge to maintain the overall neutrality of the system. The procedure that we used to set a net equivalent charge for comparison between the different systems is discussed below.

*Modeling net equivalent charges:* Due to the significant difference in the unit cell volume for the different 2D perovskite phases, a common guideline of scaling the net equivalent charges was used to induce the general effect of charge injection. An example of this discrepancy in unit cell volume is that the experimental structure of the DJ compound presents 6 inorganic  $[\text{PbI}_6]^{4-}$  octahedra with a volume of 1810.82 Å<sup>3</sup> while the experimental structure of the RP compound presents 12  $[\text{PbI}_6]^{4-}$  octahedra with a volume of 3987.67 Å<sup>3</sup>. Hence, injecting one electron into the DJ structure is not equivalent to injecting one into the RP structure. We used the number of inorganic octahedra as a guide to fix a net equivalent charge for comparison. For example, injecting one charge in the DJ structure with 6 octahedra would be equivalent to injecting 2 charges in the BA structure with 12 octahedra. The Supplementary Table 2 summarizes the number of charges used to get the net equivalent charges for the different systems. The DJ compound with 6 octahedra was used as a reference to get the conversion for the other systems based on the number of inorganic octahedra.

*Structural model:* The starting structures used in the DFT simulations were obtained from previous X-ray diffraction (XRD) measurements.<sup>1,2,3,5</sup> In the ACI compounds (n=2, 3), the first lattice parameter “a” is about 6.4 Å which potentially leads to more spurious periodic image interactions when charges are injected into the system. To minimize the latter effect, the cells were doubled

along the a-direction for both n=2 and 3 of the ACI compounds resulting in the “a” lattice parameter being about 12.8 Å. Due to the molecular positions in the XRD data which are subject to ambiguity because of their dynamic disorder, especially at room temperature, we rotated every second MA (methylammonium) molecule to 180° in each plane of the perovskite layer for the ACI compounds.<sup>4</sup> This was to minimize the net dipole in the system. Similarly, for the DJ compound, we rotated every second 4AMP organic barrier molecule to 180°. The results from the geometry optimization of the different systems are summarized in Supplementary Table 3, 4, 5, and 6. For the DJ compound, the results obtained using the experimentally reported molecular 4AMP orientations are also summarized in Supplementary Table 3b for comparison.

*Technical comment:* We note that relaxing the DJ n=3 structures using the Broyden optimization algorithm as implemented in SIESTA presents issues related to the sticking of the systems in local minima. In the case of hole injection at a charge +2, we noticed that the system got stuck at a local minimum not too far from the convergence criteria. In particular, the in-plane lattice parameter tended to be contracted at charge +2 which is in a better agreement with experiment. However, given that the convergence on the forces was not fully satisfied, it could be that the in-plane lattice parameters would exhibit a different behavior if the criteria were met as in the case of the FIRE relaxation algorithm that we adopted for this work.

### **Device simulation**

*Optical modeling:* The optical absorption for the perovskite cell was modeled using the full-wave solution of Maxwell’s equations. The transfer matrix method was used for the planar cell structure. 300 – 1500nm wavelength range was used in the calculation. Further details can be found in supplementary information in as the same simulation was used in this study.<sup>24</sup>

*Self-consistent transport simulation:* Electron and hole transportation in the solar cell was simulated by MEIDCI, a commercial device simulator software. For carrier transport equations, the generation term in the continuity equation was calculated from the photo-generated profile and the recombination term in the continuity equation was calculated for direct as well as for defect assisted Shockley-Read-Hall recombination. Effects from excitons and hot electrons were not accounted for explicitly.

*Electrical field profile:* To simulate the electric field distribution in the device, a 200nm perovskite film thickness was selected. Four quantum wells were used for the simulations. The depletion region width for the layer perovskite was from previous studies.<sup>24</sup>

#### **Data Availability**

The data for this study are available from the authors upon reasonable request.

#### **Code Availability**

The analysis code for this study is available from the authors upon reasonable request.

## Supplementary Discussion

**1. Density Functional Theory** Our DFT calculations compared the structure of the 2D perovskite crystals (DJ  $n=3$ , ACI  $n=2$ , ACI  $n=3$ , and RP  $n=3$ ) before and after the injection of a charge (electron or hole) into the lattice (Fig. 2b and Supplementary Fig. 6c). Our results show that upon electron injection, the structures of the three types of 2D perovskite (RP, ACI, DJ) exhibit out-of-plane contraction and in-plane expansion with strain of the same order in both direction, which is incompatible with our experimental results. On the other hand, the ACI perovskites' simulated structures after the injection of one or two holes exhibit anisotropic contraction of their lattice parameters with little change of the Pb-I-Pb angles (Fig. 2b and Supplementary Fig. 6d) which is in good agreement with the experiments. In DJ  $n=3$ , our modeling results agree qualitatively with the experiment for one-hole injection only by predicting mainly contraction of the structure in the out-of-plane direction without octahedra tilting and reduction of the organic interlayer spacing. For the RP perovskite, the theory predicts non-negligible strain ( $>0.1\%$ ) for both electron and hole injection, therefore suggesting that charge accumulation is negligible in the bulk in the RP  $n=3$ . Conversely, our theory confirms that the DJ and ACI perovskite structures exhibit larger lattice contraction along the stacking direction as compared to in-plane upon hole injection, which we explain by the lower out-of-plane Young's modulus. It also predicts that at equivalent injected charges the light-induced effects are more important in DJ as compared to ACI perovskites, as observed experimentally.

**2. X-ray photo-electron spectroscopy analysis.** As shown in Fig 2.c and d, Supplementary Fig. 6 a,b, we measured the XPS spectra of the Pb  $4f_{7/2}$  and I  $3d_{5/2}$  binding states. To exclude any degradation effect, we extract the iodide and lead element ratios before and after light illumination. For DJ =3 mm-sized crystal iodide and lead ratios were 58.27:20.75 versus 58.77:20.23, before and after, respectively. For DJ  $n=3$  film iodide and lead ratios were 58.27:20.75 versus 58.77:20.23, before and after, respectively. For RP =3 thin film iodide and lead ratios were 52.14:20.22 versus 52.47:20.47, before and after, respectively. For MAPI 3D thin film iodide and lead ratios were 70.83:29.17 versus 69.77:30.22, before and after, respectively. We observed no shift in the carbon binding energy in all the spectras, nor did we observe the previously reported degradation effects such as traces of metallic lead ( $Pb^0$ ) states in the DJ and MAPI<sub>3</sub> samples.

**3. Space Charge Limited Photocurrent analysis.** As shown in Fig. 3b, the space charge limited current was conducted by measuring the J-V trace of the electron only device. We scanned from 0V to 5.5V. In the linear/ohmic region, the conductivity was determined by Ohms law

$$J = \sigma E = \frac{en\mu V}{L}$$

where  $\mu$  is the mobility,  $E$  is the electric field,  $L$  is the length of active layer, and  $\sigma$  is the conductivity.<sup>24</sup> We then determine that the sublinear region of the J-V curve was the space-charge limited photocurrent regime due to the fulfillment three criteria proposed by V.D Mihailetchi et.

al, large photogenerated charge carrier generation rate  $G$ , long carrier lifetime after dissociation of exciton, the strongly unbalanced of charge transport.<sup>25</sup> The current in this region is given by the following equation

$$J_{ph} = q \left( \frac{9\varepsilon_0\varepsilon_r\mu}{8q} \right)^{\frac{1}{4}} G^{\frac{3}{4}} V^{\frac{1}{2}}$$

Where  $\varepsilon_0$  is the permittivity of free space,  $\varepsilon_r$  is the dielectric constant, which is 6 for DJ perovskite<sup>26</sup>, and  $q$  is the electron charge. The trap-filled region was identified by a 3<sup>rd</sup> order polynomial fit similar to recent reports in perovskites.<sup>24</sup>

**4. Percolation model for photo-hole trapping.** To support our hypothesis of a percolation-based mechanism, we developed percolation-model of describing the changes in the mobility. We fit the experimental percolation behavior of the electron mobility,  $\mu_e$ , as a function of time with a Boltzmann sigmoid empirical law<sup>38-40</sup>:

$$\mu_e(t) = A_{before} + \frac{A_{after} - A_{before}}{1 + e^{(t_0-t)/b}} \quad (1)$$

where  $A_x$  ( $x$  represents “before” or “after”) is the mobility before or after light illumination,  $t_0$  is the midpoint time of the sigmoid curve defined as a threshold time, and  $b$  is a parameter which allows fitting the steepness of the mobility increase around the threshold. By fitting each of the mobility curves with the same sigmoid function, we extracted the threshold time  $t_0$  and find that  $t_0$  is inversely proportional to the light intensity (Fig. 3g). We describe the onset of the percolation by balancing the rate of generation process with a depopulation process, which is summarized by the following equations:

$$C_t = t_0 G_{eff} \quad (2)$$

$$G_{eff} = (\alpha G - G_D) \quad (3)$$

Where  $G_{eff}$  is the effective trapping rate of the photogenerated holes,  $G$  is the light-induced generation rate per unit volume of photocarriers, which is proportional to the light flux ( $\text{cm}^{-3}/\text{s}$ ),  $\alpha$  is the photo-hole capture coefficient ( $\text{cm}^3$ ), and  $G_D$  is the depopulation rate of the trapped carriers ( $1/\text{s}$ ). Based on the experimental results in Fig. 4e, we assume that the percolation threshold time  $t_0$  is simply inversely proportional to effective generation rate, through a constant  $C_t$ . This constant represents the total number of filled iodide trap sites (unitless) needed to reach the percolation threshold.

$$C_t = t_0 G_{eff} \quad (2)$$

From the fit, we extracted a threshold  $C_t$  to be  $1.86 \times 10^7$  (number of iodide sites), a capture coefficient  $\alpha$  to be  $2.84 \times 10^{-16} \text{ cm}^{-3}$ , and a depopulation density to be  $G_D$   $1.96 \times 10^5 \text{ s}^{-1}$ . We note that the introduction of a depopulation (carrier detrapping) rate is necessary to reproduce the experimental recovery of the initial mobility once the illumination is switched off (vide infra). Furthermore, in classical semiconductor physics, the physical analogue of  $\alpha$  is the carrier capture rate in a recombination and generation (R-G) process for semiconductors and is related capture cross section ( $\sigma_p$ ) of a recombination site (defect).<sup>41</sup> In our photogenerated hole trapping system, the iodide sites are the recombination centers and  $\sigma_p$  is the area of an iodide atom (is on the order of  $10^{-16} \text{ cm}^2$ ). Additionally, we note that the depopulation rate  $G_D$  is lower than the generation rate times capture coefficient ( $\alpha G$ ) since we observed a sigmoidal increase for all the light fluxes. From the two equations above, we rewrite the mobility as a function of generation and depopulation rate:

$$\mu_e(t) = A_{dark} + \frac{A_{light} - A_{dark}}{1 + e^{\left(\frac{C_t}{b(\alpha G - G_D)} - \frac{t}{b}\right)}} \quad (4)$$

This model is in excellent agreement with our flux dependent SCLC measurements (Fig. 4d). For example, at low fluxes (0.5-Sun and 1-Sun) the midpoint time of growth is large ( $t_0 > 20$  minutes) due to the fact that the generation rate is on the same order as the depopulation rate ( $\alpha G \cong G_D$ ). At high flux (5-suns) where  $G \gg G_D$ , the midpoint time of increase is small ( $t_0 \cong 1$  minutes). We further verify the percolation model by plotting the dependence of midpoint time of rise against the number of photogenerated carriers ( $G$ ). Not surprisingly, we find that  $t_0$  is inversely proportional to  $G$  (Supplementary Fig. 8c) and can be fitted to a rearranged threshold equation from above.

$$G = \alpha \left( \frac{C_t}{t_0} + G_D \right) \quad (5)$$

Moreover, we can plot the electron mobility trend as a function of number of trapped holes by using the threshold equation and the fitted values.

$$\text{Number of carriers} = t(\alpha G - G_D) \quad (6)$$

Lastly, the percolation model can also predict the behavior of the mobility relaxation back to its initial value once the illumination is switched off (see Supplementary Fig. 8d for relaxation in dark). The relaxation trend is described by the same law but removing the generation term  $\alpha G$ , in the dark. We also note that the typical relaxation time of the sample conductivity is on the same order as the one describing the build-up of the electrical percolation process. They are both characteristic of the collective electrical interconnection of the conductive domains inside the crystal and are not compared to time scales relevant for single hole excitation or relaxation.

**Supplementary Table 1** | Summary of the experimental values of both the lattice parameters and unit cell volume measured before and after 51 minutes of continuous light illumination of the samples.

	<i>Out-of-plane parameter</i>			<i>In-plane parameters</i>			<i>Volume</i>		
	Before (Å)	After (Å)	Strain (%)	Before (Å)	After (Å)	Strain (%)	Before (Å <sup>3</sup> )	After (Å <sup>3</sup> )	Change (%)
DJ <i>n</i> =3	23.12	22.90	0.95	8.85	8.80	0.56	1810.82	1773.38	2.07
ACI <i>n</i> =3	43.23	42.98	0.57	6.27	6.24	0.48	3398.99	3347.07	1.55
ACI <i>n</i> =2	31.27	31.01	0.83	6.28	6.25	0.46	2466.47	2422.65	1.81
RP <i>n</i> =3	50.57	50.57	0.00	8.88	8.88	0.00	3987.67	3987.67	0.00

**Supplementary Table 2** | Convention for calculating the net equivalent charges injected in the perovskite systems for the first principle calculations. The 6 octahedra for the DJ compound were used as a reference.  $\frac{q_{DJ}}{N_{DJ}} = \frac{q_x}{N_x}$  where  $N_{DJ} = 6$  (6 octahedra for DJ),  $q_{DJ}$  number of injected charges into the DJ,  $N_x$  number of octahedra of the compound for which we would like to obtain the number of injected charges  $q_x$ .

	Number of inorganic octahedral	Number of injected charges	Net equivalent charge
DJ <i>n</i> =3	6	1	1
	6	2	2
ACI <i>n</i> =2	16	8/3	1
	16	16/3	2
ACI <i>n</i> =3	24	4	1
	24	8	2
RP <i>n</i> =3	12	2	1
	12	4	2

**Supplementary Table 3a** | DFT computed structural change in the DJ  $n=3$  perovskite for neutral and charged states. Relaxed lattice parameters for the DJ perovskite after charge injection. The percentage error with respect to the reference neutral system is shown between parentheses. The out-of-plane and in-plane directions correspond to the a-axis and bc-plane, respectively.

		Lattice parameters					
	Equivalent net charge	a(Å)	b(Å)	c(Å)	$\beta(^{\circ})$	Volume (Å <sup>3</sup> )	<interlayer I-I> (Å)
Reference neutral	0	22.8729	9.1124	8.2718	90	1724.08	3.88
charged systems	1-	22.8555 (-0.1%)	9.1515 (+0.4%)	8.2781 (+0.1%)	90	1731.45 (+0.4%)	3.86 (-0.5%)
	2-	22.8538 (-0.1%)	9.1979 (+0.9%)	8.2880 (+0.2%)	90	1742.19 (+1.1%)	3.81 (-1.8%)
	--	--	--	--	--	--	--
	1+	22.7765 (-0.4%)	9.1019 (-0.1%)	8.2677 (-0.0%)	90	1713.97 (-0.6%)	3.86 (-0.5%)
	2+	22.3423 (-2.3%)	9.1117 (-0.0%)	8.3281 (+0.7%)	90	1695.61 (-1.7%)	3.62 (-6.7%)

**Supplementary Table 3b** | DFT computed structural change in the DJ  $n=3$  perovskite for neutral and charged states. Relaxed lattice parameters for the DJ perovskite after charge injection. The percentage error with respect to the reference neutral system is shown between parenthesis. The out-of-plane and in-plane directions correspond to the a-axis and bc-plane, respectively.

		Lattice parameters					
	Equivalent net charge	a(Å)	b(Å)	c(Å)	$\beta(^{\circ})$	Volume (Å <sup>3</sup> )	<interlayer I-I> (Å)
Reference neutral	0	22.8956	9.0697	8.3146	90	1726.57	3.92
charged systems	1-	22.8523 (-0.2%)	9.1291 (+0.7%)	8.3284 (+0.2%)	90	1737.48 (+0.6%)	3.87 (-1.3%)
	2-	22.8422 (-0.2%)	9.1722 (+1.1%)	8.3339 (+0.2%)	90	1746.07 (+1.1%)	3.83 (-2.3%)
	--	--	--	--	--	--	--
	1+	22.7652 (-0.6%)	9.052 (-0.2%)	8.3077 (-0.1%)	90	1711.96 (-0.8%)	3.89 (-0.8%)
	2+	22.2956 (-2.6%)	9.0829 (+0.1%)	8.3847 (+0.8%)	90	1697.96 (-1.7%)	3.60 (-8.2%)

**Supplementary Table 4** | DFT computed structural change in ACI  $n=2$  perovskite for neutral and charged states. Relaxed lattice parameters for the ACI perovskite after charge injection. The percentage error with respect to the reference neutral system is shown between parenthesis. The out-of-plane and in-plane directions correspond to the b-axis and ac-plane, respectively.

		Lattice parameters							
	Equivalent net charge	a(Å)	b(Å)	c(Å)	$\beta(^{\circ})$	Volume (Å <sup>3</sup> )	<interlayer I-I> (Å)		
							average	min	max
Reference neutral	0	12.6346	30.7063	12.3242	90	4781.29	4.26	3.92	4.47
charged systems	1-	12.7301 (+0.7%)	30.6429 (-0.2%)	12.3356 (+0.1%)	90	4811.94 (+0.6%)	4.25 (-0.2%)	3.91	4.46
	2-	12.8013 (+1.3%)	30.3366 (-1.2%)	12.4521 (+1.0%)	90	4835.74 (+1.1%)	4.19 (-1.6%)	3.88	4.41
	--	--	--	--	--	--	--	--	--
	1+	12.5903 (-0.4%)	30.6180 (-0.3%)	12.3038 (-0.2%)	90	4742.99 (-0.8%)	4.27 (+0.2%)	3.89	4.47
	2+	12.5375 (-0.8%)	30.5143 (-0.6%)	12.3098 (-0.1%)	90	4709.40 (-1.5%)	4.26 (0%)	3.78	4.51

**Supplementary Table 5** | DFT computed structural change in ACI  $n=3$  perovskite for neutral and charged states. Relaxed lattice parameters for the ACI perovskite after charge injection. The percentage error with respect to the reference neutral system is shown between parenthesis. The out-of-plane and in-plane directions correspond to the c-axis and ab-plane, respectively.

	Equivalent net charge	Lattice parameters				Volume ( $\text{\AA}^3$ )	<interlayer I-I> ( $\text{\AA}$ )		
		a( $\text{\AA}$ )	b( $\text{\AA}$ )	c( $\text{\AA}$ )	$\beta(^{\circ})$		average	min	max
Reference neutral	0	12.6686	12.3611	43.0639	90	6743.6887	4.25	4.02	4.47
charged systems	1-	12.7923 (+1.0%)	12.3895 (+0.2%)	42.7700 (-0.7%)	90	6778.62 (+0.5%)	4.22 (-0.7%)	4.02	4.46
	2-	12.8681 (+1.6%)	12.4700 (+0.9%)	42.4982 (-1.3%)	90	6819.46 (+1.1%)	4.19 (-1.4%)	4.01	4.41
	--	--	--	--	--	--	--	--	--
	1+	12.6379 (-0.2%)	12.3212 (-0.3%)	42.9072 (-0.4%)	90	6681.27 (-0.9%)	4.24 (-0.2%)	4.02	4.49
	2+	12.5992 (-0.5%)	12.3017 (-0.5%)	42.7532 (-0.7%)	90	6626.39 (-1.7%)	4.25 (0%)	4.02	4.51

**Supplementary Table 6** | DFT computed structural change in RP  $n=3$  perovskite for neutral and charged states. Relaxed lattice parameters for the RP perovskite after charge injection. The percentage error with respect to the reference neutral system is shown between parenthesis. The out-of-plane and in-plane directions correspond to the b-axis and abc-plane, respectively.

		Lattice parameters					
	Equivalent net charge	a(Å)	b(Å)	c(Å)	$\beta(^{\circ})$	Volume (Å <sup>3</sup> )	<interlayer I-I> (Å)
Reference neutral	0	8.3388	52.4942	9.1261	90	3994.82	> 7
charged systems	1-	8.3561 (+0.2%)	52.5199 (+0.0%)	9.1660 (+0.4%)	90	4022.62 (+0.7%)	> 7
	2-	8.3333(- 0.1)	52.1980 (-0.6%)	9.2927 (+1.8%)	90	4042.13 (+1.2%)	> 7
	--	--	--	--	--	--	--
	1+	8.330 (- 0.1%)	52.4340 (-0.1%)	9.0784 (-0.5%)	90	3965.56 (-0.7%)	> 7
	2+	8.3255(- 0.2%)	52.3146 (-0.3%)	9.0282 (-1.1%)	90	3932.14 (-1.6%)	> 7

**Supplementary Table 7** | Comparison of the figures of merit of the DJ and ACI perovskite solar cells between the experimental data (Exp.) and device model (Sim.).

<b>Before</b>	<b>Perovskite</b>	<b>Jsc (mA.cm<sup>-2</sup>)</b>	<b>Voc (V)</b>	<b>FF</b>	<b>PCE (%)</b>
Sim.	DJ <i>n</i> =4	16.18	1.02	0.69	7.99
Expr.	DJ <i>n</i> =4	17.54	1.02	0.72	12.85
Sim.	ACI <i>n</i> =3	14.86	0.92	0.59	7.99
Expr.	ACI <i>n</i> =3	14.79	0.91	0.60	8.04
<b>After</b>	—	—	—	—	—
Sim.	DJ <i>n</i> =4	16.22	1.10	0.76	13.58
Expr.	DJ <i>n</i> =4	17.47	1.10	0.86	16.45
Sim.	ACI <i>n</i> =3	15.00	1.02	0.75	11.55
Expr.	ACI <i>n</i> =3	14.35	1.01	0.76	11.07

**Supplementary Table 8** | Equations for Carrier Transport used in the solar cell device model.<sup>10</sup>

Poisson Equation: $\epsilon_r \epsilon_0 \nabla^2 \psi = -q (n_h - n_e)$ Continuity: $\nabla J_{e,h} = (G_{e,h} - R_{e,h}(n_e, n_h))$ Drift-Diffusion: $J_{e,h} = \mu_{e,h} n_{e,h} (-\nabla \psi) \pm D_{e,h} \nabla n_{e,h}$ Recombination: $R_{e,h}(n_e, n_h) = B(n_e n_h - n_i^2) + \frac{n_e n_h - n_i^2}{\tau(n_e + n_h)}$
--

**Supplementary Table 9** | Absorber parameters for ACI  $n=3$  used in the device model.<sup>28-30</sup> “Before” and “after” corresponding to the parameters used before illumination and after 11 minutes under illumination.

Symbol	Description	Parameter value
$L_{Absorber}$	Thickness of absorber layer	200 nm
$\mu_e$	Electron mobility in absorber	<b>Before:</b> 10 (cm <sup>2</sup> /V.s) <b>After:</b> 30 (cm <sup>2</sup> /V.s)
$\mu_h$	Hole mobility in absorber	<b>Before:</b> 10 (cm <sup>2</sup> /V.s) <b>After:</b> 30 (cm <sup>2</sup> /V.s)
$\tau_e$	Electron lifetime in absorber	10 (ns)
$\tau_h$	Hole lifetime in absorber	10 (ns)
$LUMO$	Lowest Unoccupied Molecular Orbital	<b>Before:</b> 3.72 (eV) <b>After:</b> 3.82 eV
$E_G$	Band gap of absorber	1.73 (eV)
$\epsilon_r$	Relative dielectric constant	25
$N_A$	Self-Doping concentration (P-type)	$1 * 10^{16}$ (#/cm <sup>3</sup> )

**Supplementary Table 10** | Absorber parameters of DJ  $n=4$  used in the device model. “Before” and “after” corresponding to the parameters used before illumination and after 11 minutes under illumination.

Symbol	Description	Parameter value
$L_{Absorber}$	Thickness of absorber layer	200 nm
$\mu_e$	Electron mobility in absorber	<b>Before:</b> 10 (cm <sup>2</sup> /V.s) <b>After:</b> 30 (cm <sup>2</sup> /V.s)
$\mu_h$	Hole mobility in absorber	<b>Before:</b> 10 (cm <sup>2</sup> /V.s) <b>After:</b> 30 (cm <sup>2</sup> /V.s)
$\tau_e$	Electron lifetime in absorber	10 (ns)
$\tau_h$	Hole lifetime in absorber	10 (ns)
$LUMO$	Lowest Unoccupied Molecular Orbital	<b>Before:</b> 3.72 (eV) <b>After:</b> 3.81 (eV)
$E_G$	Band gap of absorber	1.72 (eV)
$\epsilon_r$	Relative dielectric constant	25
$N_A$	Self-Doping concentration (P-type)	$10^{16}$ (#/cm <sup>3</sup> )

**Supplementary Table 11** | Electron transport material parameters (ETM = C60)<sup>31</sup>

Symbol	Description	Parameter value
$L_{ETM}$	Thickness of ETM layer	30 nm
$\mu_e$	Electron mobility in ETM	$10^{-2}$ (cm <sup>2</sup> /V.s)
$\mu_h$	Hole mobility in ETM	$10^{-2}$ (cm <sup>2</sup> /V.s)

$\tau_e$	Electron lifetime in ETM	1000 (ns)
$\tau_h$	Hole lifetime in ETM	1000 (ns)
<i>LUMO</i>	Lowest Unoccupied Molecular Orbital	4.33 (eV)
$E_G$	Band gap of ETM	2.0 (eV)
$\epsilon_r$	Relative dielectric constant	4
$N_D$	Self-Doping concentration (N-type)	$5 * 10^{17}$ (#/cm <sup>3</sup> )

**Supplementary Table 12** | Hole transport material parameters (HTM = PEDOT:PSS)<sup>32,33</sup>

Symbol	Description	Parameter value
$L_{HTM}$	Thickness of HTM layer	30 nm
$\mu_e$	Electron mobility in HTM	$9 * 10^{-3}$ (cm <sup>2</sup> /V.s)
$\mu_h$	Hole mobility in HTM	$9 * 10^{-3}$ (cm <sup>2</sup> /V.s)
$\tau_e$	Electron lifetime in HTM	1000 (ns)
$\tau_h$	Hole lifetime in HTM	1000 (ns)
<i>HUMO</i>	Highest Occupied Molecular Orbital	5.18 (eV)
$E_G$	Band gap of HTM	1.55 (eV)
$\epsilon_r$	Relative dielectric constant	3
$N_A$	Self-Doping concentration (P-type)	$3 * 10^{17}$ (#/cm <sup>3</sup> )

**Supplementary Table 13** | Electron transport material parameters (ETM = PCBM)<sup>35-37</sup>

Symbol	Description	Parameter value
$L_{ETM}$	Thickness of ETM layer	30 nm

$\mu_e$	Electron mobility in ETM	$10^{-2}$ (cm <sup>2</sup> /V.s)
$\mu_h$	Hole mobility in ETM	$10^{-2}$ (cm <sup>2</sup> /V.s)
$\tau_e$	Electron lifetime in ETM	1000 (ns)
$\tau_h$	Hole lifetime in ETM	1000 (ns)
$LUMO$	Lowest Unoccupied Molecular Orbital	4.23 (eV)
$E_G$	Band gap of ETM	2.0 (eV)
$\epsilon_r$	Relative dielectric constant	4
$N_D$	Self-Doping concentration (N-type)	$5 * 10^{17}$ (#/cm <sup>3</sup> )

**Supplementary Table 14** | Bathocuproine layer parameters used in the device model.<sup>31</sup>

Symbol	Description	Parameter value
$L_{ETM}$	Thickness of ETM layer	1 nm
$\mu_e$	Electron mobility in ETM	$10^{-4}$ (cm <sup>2</sup> /V.s)
$\mu_h$	Hole mobility in ETM	$10^{-4}$ (cm <sup>2</sup> /V.s)
$\tau_e$	Electron lifetime in ETM	1000 (ns)
$\tau_h$	Hole lifetime in ETM	1000 (ns)
$LUMO$	Lowest Unoccupied Molecular Orbital	4.00 (eV)
$E_G$	Band gap of ETM	3.5 (eV)
$\epsilon_r$	Relative dielectric constant	4
$N_D$	Self-Doping concentration (N-type)	$5 * 10^{17}$ (#/cm <sup>3</sup> )

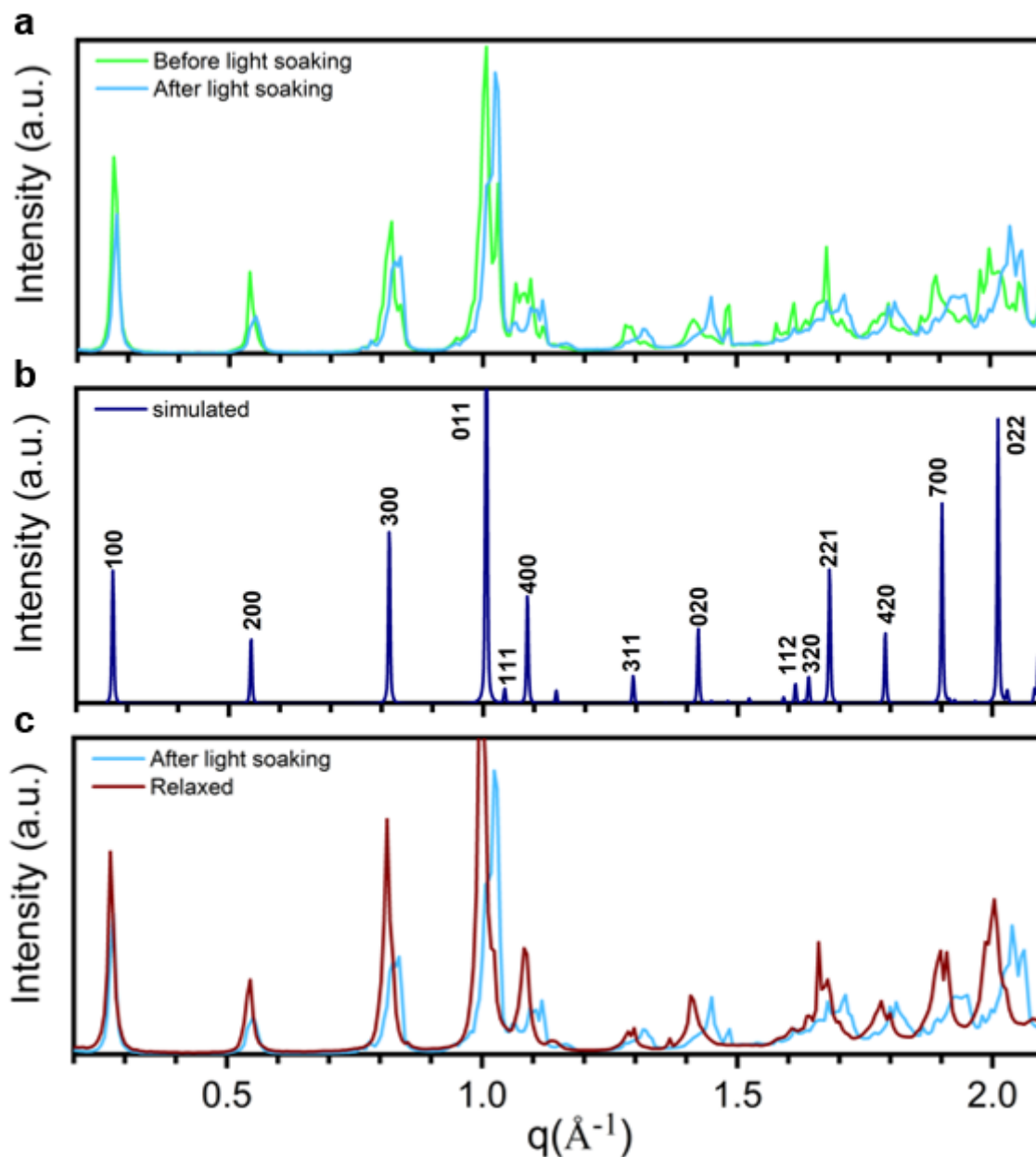
## Additional reference

1. Stoumpos C. *et al.* Ruddlesden–Popper Hybrid Lead Iodide Perovskite 2D Homologous Semiconductors. *Chem. Mater.* **28**, 2852–2867. (2016)
2. Soe, C. M. M. *et al.* Structural and thermodynamic limits of layer thickness in 2D halide perovskites. *Proceedings of the National Academy of Sciences*, **116**, 58–66 (2019)
3. Mao, L. *et al.* Hybrid Dion–Jacobson 2D Lead Iodide Perovskites. *J. Am. Chem. Soc.* **140**, 3775–3783 (2018)
4. Soe, C. M. M. *et al.* New type of 2D perovskites with Alternating Cations in the Interlayer space,  $(\text{C}(\text{NH}_2)_3)(\text{CH}_3\text{NH}_3)_n\text{Pb}_n\text{I}_{3n+1}$ : Structure, Properties, and Photovoltaic Performance. *J. Am. Chem. Soc.* **139**, 16297–16309 (2017)
5. He, X. *et al.* Oriented Growth of Ultrathin Single Crystals of 2D Ruddlesden–Popper Hybrid lead Iodide Perovskite for High-Performance Photodetector. *ACS Appl. Mater. Interfaces.* **11**, 15905–15912 (2019)
6. Sanchez-Bajo, R. and Cumbreira, F.L. The use of the Pseudo-Voigt function in Variance Method of X-ray Line-Broadening Analysis. *J. Applied Crystallography.* **30**, 427–430 (1997)
7. Jiang, Z. *et al.* The dedicated high-resolution grazing-incidence X-ray scattering beamline 8-ID-E at the Advanced Photon Source. *J. Synchrotron Radiat.* **19**, 627–636 (2012)
8. Kevin, Y., *et al.* SciAnalysis. <https://github.com/CFN-softbio/SciAnalysis>
9. A.L. Patterson, The Scherrer Formula for X-ray Particle Size Determination. *Phys. Rev.* **56**, 10, 978–982, (2019)
10. Smilgies, D-M. Scherrer grain-size analysis adapted to grazing incidence scattering with area detectors. *J. Appl Crystallography.* **42**, 1030–1034, (2009)
11. Conings, B. *et al.* Intrinsic Thermal Instability of Methylammonium Lead Trihalide Perovskite. *Adv Energy Mat.* **5**, 1500477–1500485 (2015)
12. Nam, J.K., *et al.* Potassium Incorporation for Enhanced Performance and Stability of Fully Inorganic Cesium Lead Halide Perovskite Solar Cells. *Nano Letters*, **17**, 2028–2033 (2017)
13. Hohenberg, P. and Kohn, W., Inhomogeneous Electron Gas. *Phys. Rev.* **136**, B864–B871 (1964)
14. Kohn, W. and Sham, L. J. Self-Consistent Equations Including Exchange and Correlation Effects. **140**, A1133–A1138 (1965)
15. Soler, J. M., *et al.* The SIESTA method for *ab initio* order-*N* materials simulation. *J. Phys. Condens. Matter.* **14**, 2745 (2002)
16. Cooper, V.W. Van der Waals density functional: An appropriate exchange functional. *Phys. Rev. B.* **81**, 161104. (2010)
17. Hamada, I and Otani, M. Comparative van der Waals density functional study of graphene on metal surfaces. *Rev. B.* **82**, 153412. (2010)
18. Yuk, S.F. *et al.* Towards an accurate description of perovskite ferroelectrics: exchange and correlations effects. *Scientific Reports*, **7**, 1738, (2017)

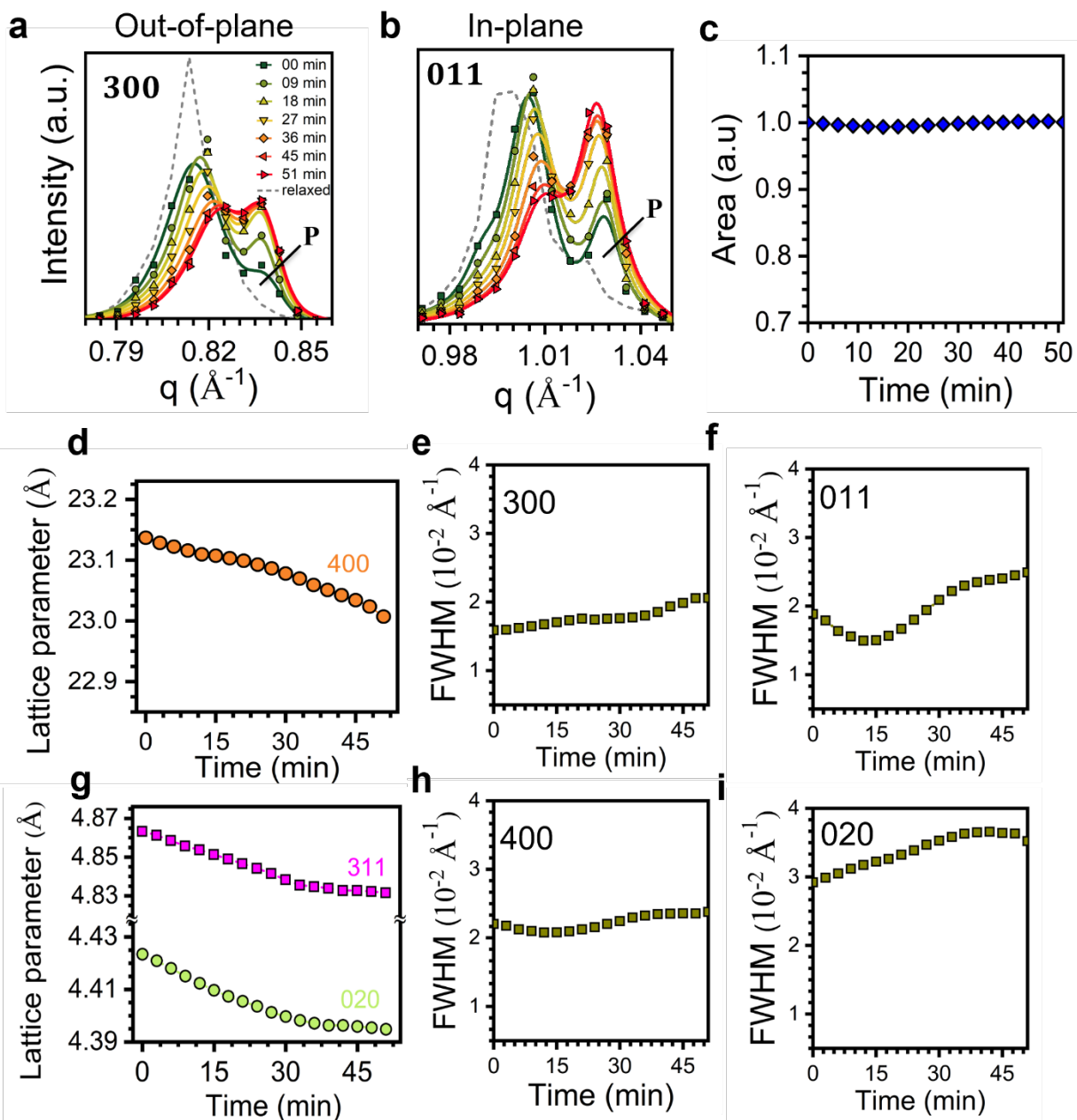
19. Boubacar, T. *et al.* Importance of Vacancies and Doping in Hole-Transporting Nickel Oxide Interface with Halide Perovskites. *ACS Appl. Mater. Interface*, **12**, 5, 6633-6640 (2020)
20. Troullier, N and Martins, J. L. Efficient pseudopotentials for plane-wave calculations. *Phys. Rev. B*, **43**, 1993-2006 (1991)
21. Bitzek, E. *et al.* Structural relaxation made simple. *Phys. Rev. Letter*, **97**, 170201 (2006)
22. Pedesseau, L. *et al.* Advances and Promises of Layered Halied Perovskite Semiconductors. *ACS Nano*, **10**, 11, 9776-9786, (2016)
23. Boubacar, T. *et al.* Composite Nature of Layered Hybrid Perovskites: Assessment on Quantum and Dielectric Confinements and Band Alignment. *ACS Nano*, **12**, 4, 3321-3332 (2018)
24. Mihailetschi, V. D., Wildeman, J. & Blom, P. W. M. Space-Charge Limited Photocurrent. *Phys. Rev. Lett.* **94**, 126602 (2005).
25. Shi, D. *et al.* Low trap-state density and long carrier diffusion in organolead trihalide perovskite single crystals. *Science* **347**, 519–522 (2015).
26. Song, B. *et al.* Determination of Dielectric Functions and Exciton Oscillator Strength of Two-Dimensional Hybrid Perovskites. *ACS Mater. Lett.* **3**, 148–159 (2021).
27. Tsai, H. *et al.* Design principles for electronic charge transport in solution-processed vertically stacked 2D perovskite quantum wells. *Nat. Comm.* **9**, 2130 (2018)
28. Stranks, S. D. *et al.* Electron-Hole Diffusion Lengths Exceeding 1 Micrometer in an Organometal Trihalide Perovskite Absorber. *Science*, **342**, 341 (2013).
29. Brivio, F. *et al.* Structural and electronic properties of hybrid perovskites for high-efficiency thin-film photovoltaics from first-principles. *APL Mater.* **1**, 042111 (2013).
30. Schulz, P. *et al.* Interface energetics in organo-metal halide perovskite-based photovoltaic cells. *Energy Environ. Sci.* **7**, 1377-1381 (2014).
31. Huang, J. *et al.* Detailed analysis of bathocuproine layer for organic solar cells based on copper phthalocyanine and C60. *Journal of Applied Physics*, vol. 105, no. 7, p. 073105, Apr. 2009, doi: 10.1063/1.3103328.
32. Lenz, A. *et al.* The electronic structure and reflectivity of PEDOT:PSS from density functional theory. *Chem. Phys.* **384**, 44-51 (2011).
33. Rutledge, S. A. and Helmy, A. S. Carrier mobility enhancement in poly(3,4-ethylenedioxythiophene)-poly(styrenesulfonate) having undergone rapid thermal annealing. *J. Appl. Phys.* **114**, 133708 (2013).
34. Trukhanov, V. A. *et al.* Effect of doping on performance of organic solar cells. *Phys. Rev. B* **84**, 205318 (2011).
35. Larson, B. W. *et al.* Electron Affinity of Phenyl–C61–Butyric Acid Methyl Ester (PCBM). *J. Phys. Chem. C* **117**, 14958-14964 (2013)
36. Guan, Z-L. *et al.* Direct determination of the electronic structure of the poly(3-hexylthiophene):phenyl-[6,6]-C61 butyric acid methyl ester blend. *Org. Electron.* **11**, 1779-1785 (2010).

37. Veldman, D. *et al.* Compositional and Electric Field Dependence of the Dissociation of Charge Transfer Excitons in Alternating Polyfluorene Copolymer/Fullerene Blends. *J. Am. Chem. Soc.* **130**, 7721-7735 (2008).
38. Bubnova, O. & Crispin, X. Towards polymer-based organic thermoelectric generators. *Energy Environ. Sci.* **5**, 9345–9362 (2012).
39. Crispin, X. *et al.* The Origin of the High Conductivity of Poly(3,4-ethylenedioxythiophene)–Poly(styrenesulfonate) (PEDOT–PSS) Plastic Electrodes. *Chem. Mater.* **18**, 4354–4360 (2006).
40. Nevrel, J. *et al.* Secondary doping in poly(3,4-ethylenedioxythiophene):Poly(4-styrenesulfonate) thin films. *J. Polym. Sci. Part B Polym. Phys.* **53**, 1139–1146 (2015)
41. Pierret, R.F. *Advanced Semiconductor Fundamentals*, 150-155, Prentice Hall, (2002).
42. Sidhik, S. *et al.* Memory Seeds Enable High Structural Phase Purity in 2D Perovskite Films for High-Efficiency Devices, *Adv. Mat.*, **33**, 2007176-2007187 (2021).

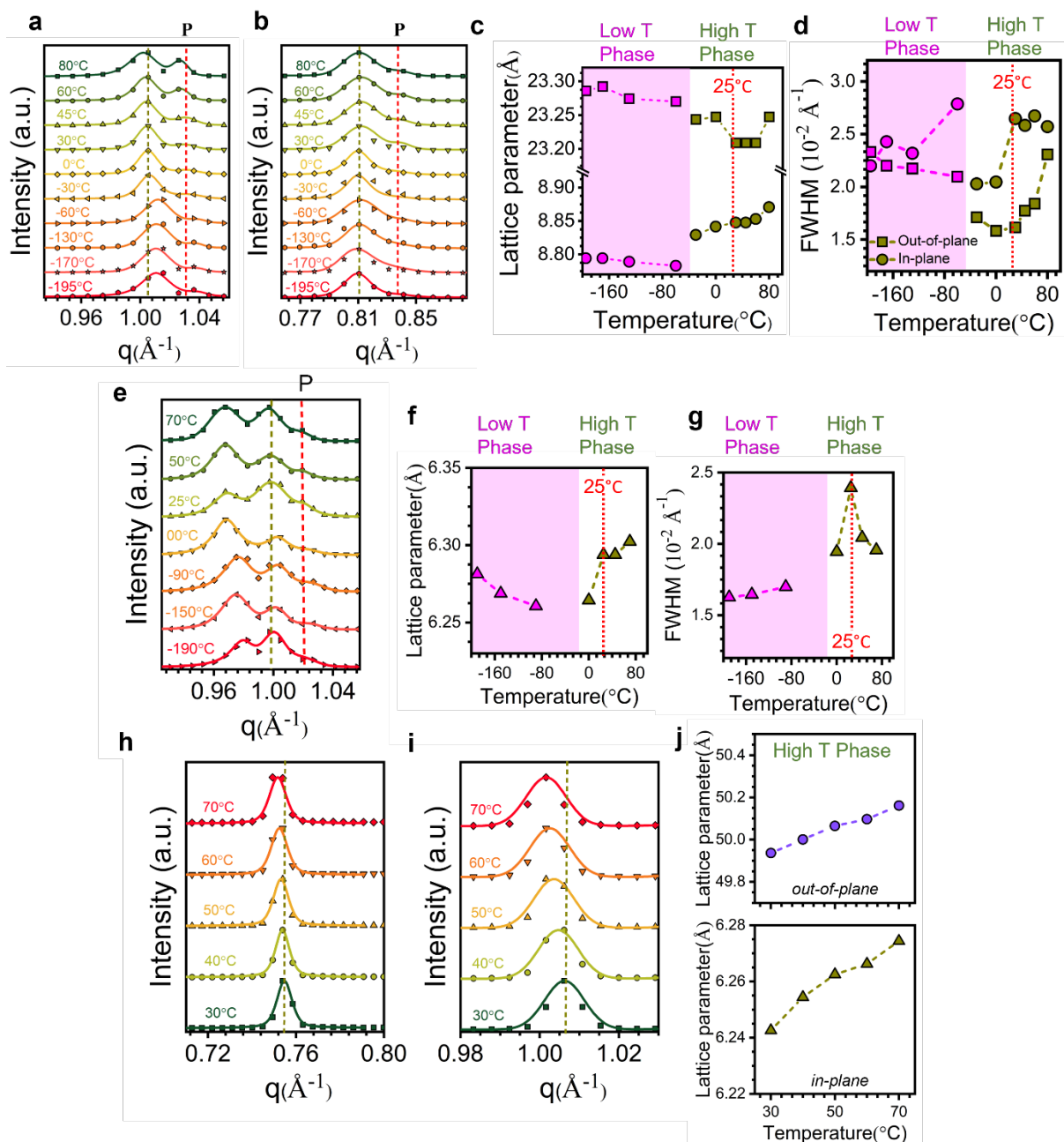
## Supplementary Figures



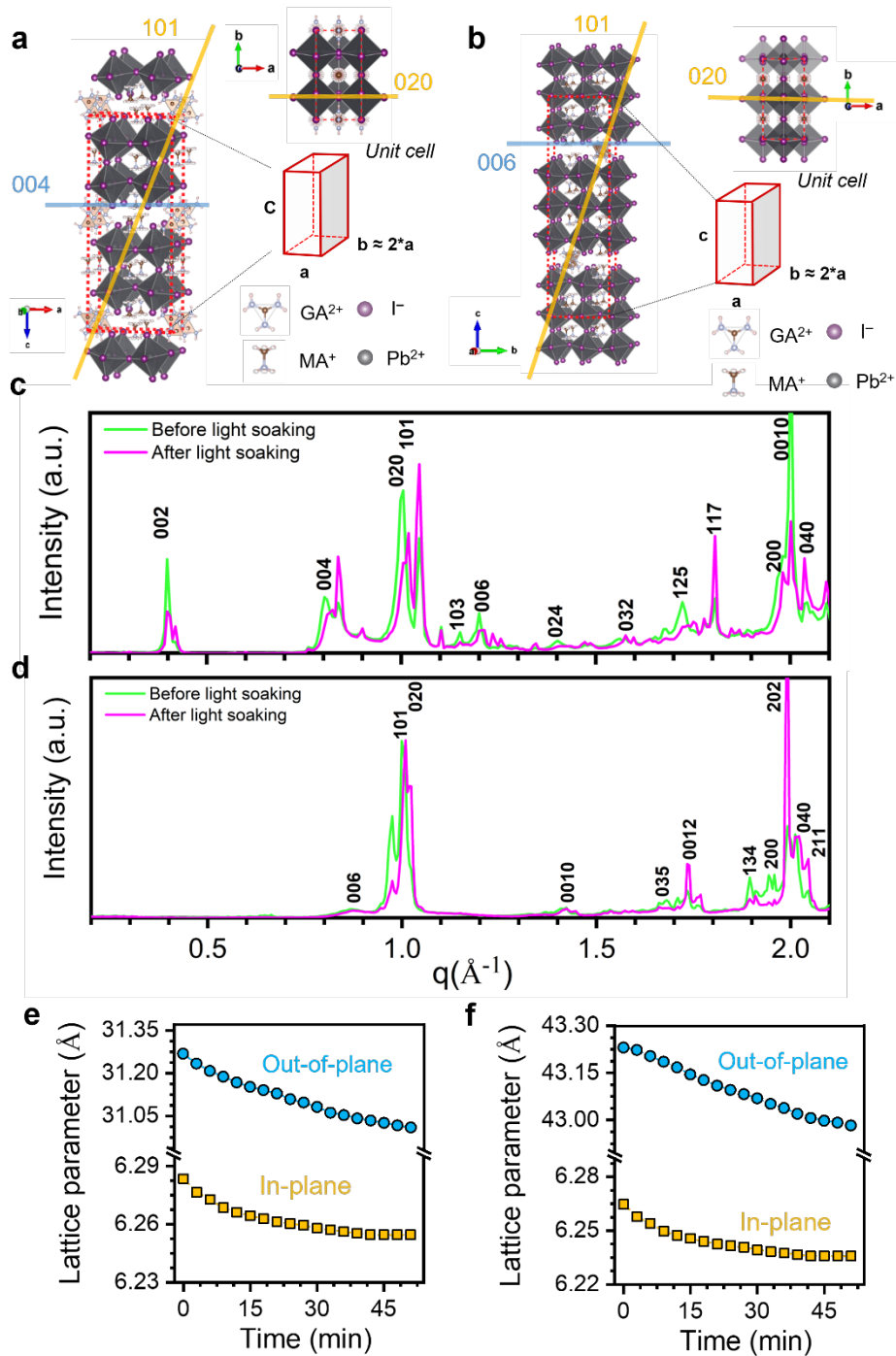
**Supplementary Fig. 1 | Structural characterization of Dion-Jacobson (4AMP)MA<sub>2</sub>Pb<sub>3</sub>I<sub>10</sub> perovskite (DJ *n*=3) powders under continuous sunlight illumination. a, Angular-integrated diffraction spectra before and after continuous light illumination for 51 minutes. b, Simulated diffraction pattern from the standard crystal structure found in ref. (3). The Miller indices hkl are labeled on the graph. c, Comparison of the diffraction spectra after 51 minutes illumination and after subsequently resting the samples in the dark for 24 hours.**



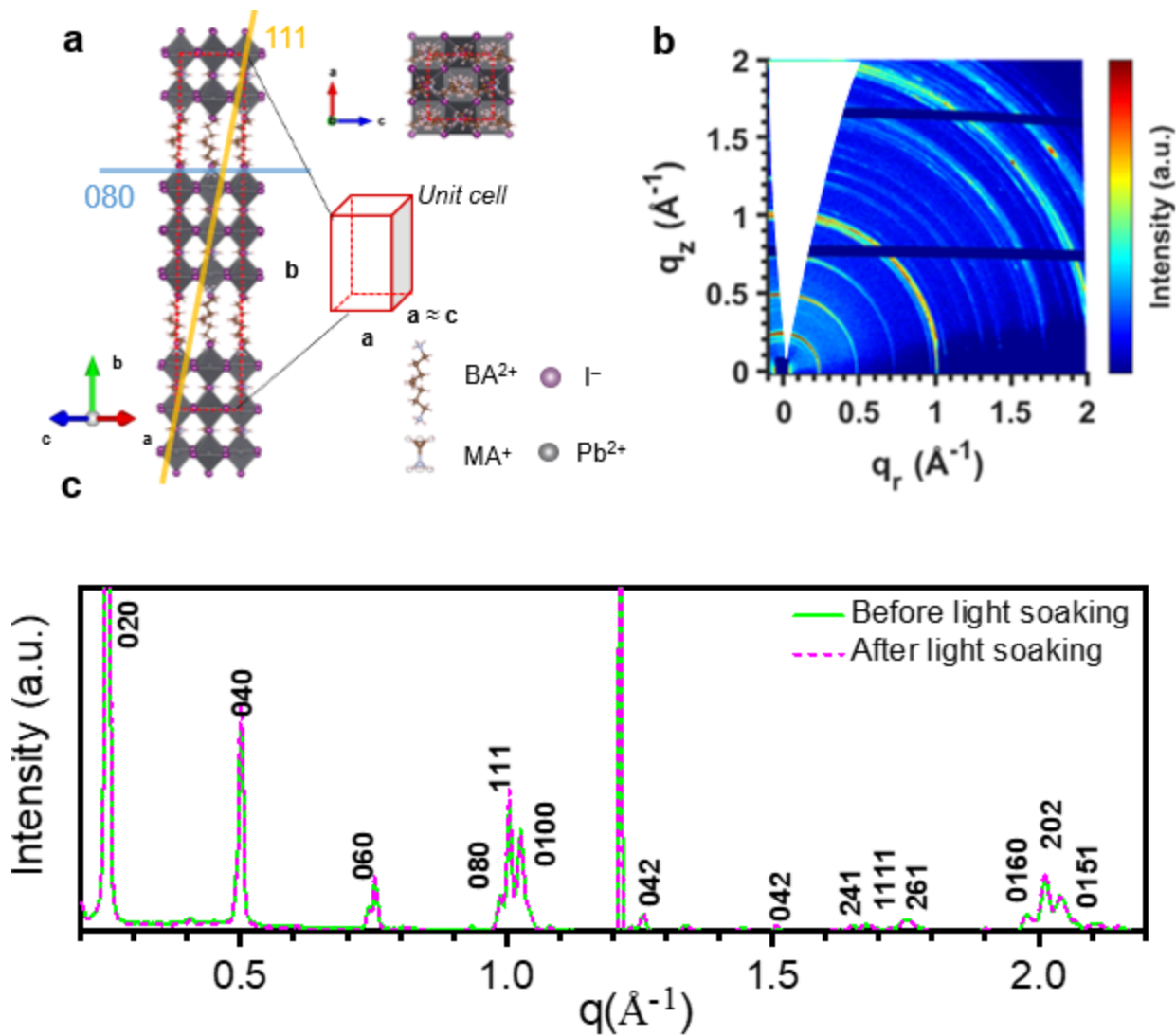
**Supplementary Fig. 2 | Extended structural analysis of the DJ  $n=3$  under light illumination.** **a**, Diffraction spectra of the (300) Bragg peak as a function of illumination time. **b**, Diffraction spectra of the (011) Bragg peak as a function of illumination time. The (300) and (011) correspond to the out-of-plane and in-plane directions of the crystals, respectively. “P” indicates the peaks corresponding to a polymorph of DJ  $n=3$ . The dash line indicates the relaxed spectra. The fits are the solid line and the data is the symbols. **c**, Evolution of the full diffraction intensity of the DJ  $n=3$  samples under constant light illumination. **d and g**, Evolution of out-of-plane and in-plane lattice parameters for the (400), (311) and (020) peaks. **e**, Progression of the full-width-at-half-max for the (300) diffraction plane. **f, h, and i**, are the same as **c** for the (011), (400), and (020) planes, respectively.



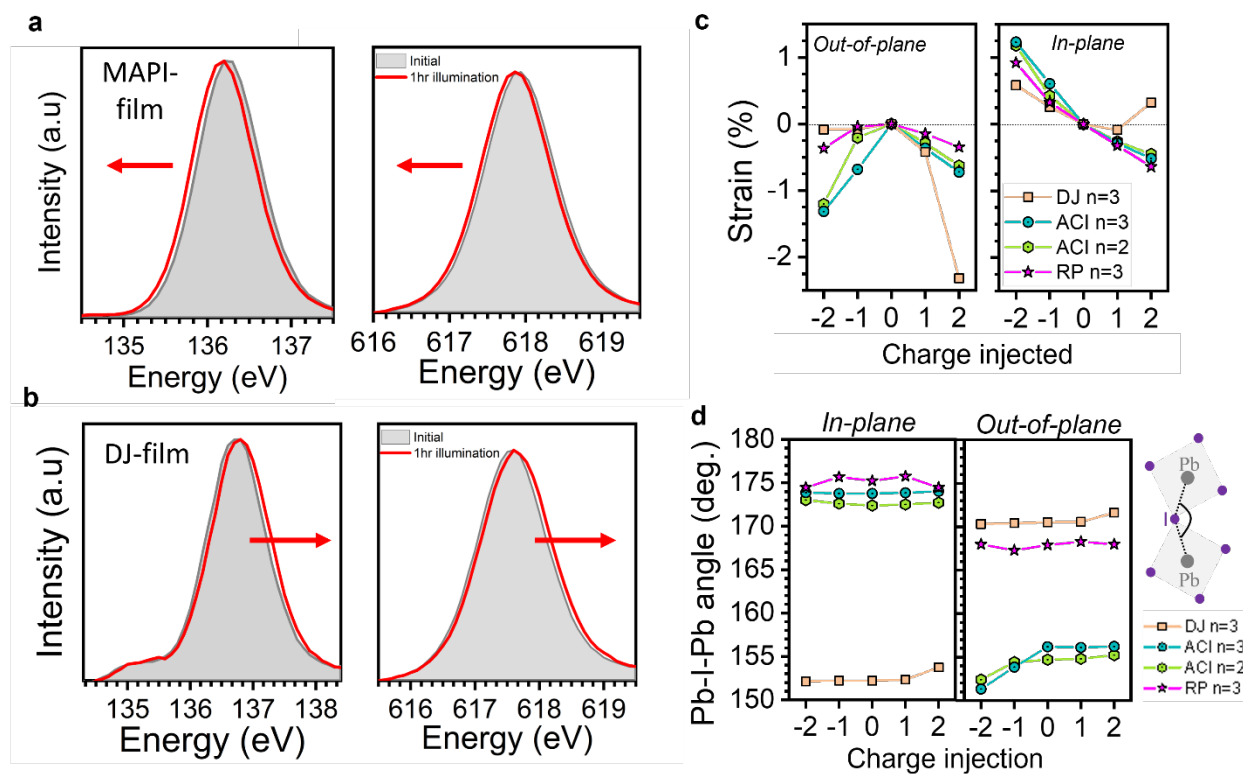
**Supplementary Fig. 3 | Temperature dependence of 2D Perovskites.** **a and b** Temperature dependent of DJ  $n=3$  powder diffraction spectra of the (011) (**a**) and (300) (**b**) planes. **c and d** Corresponding lattice parameter and full-width-at-half-maximum evolution of the out-of-plane and in-plane diffraction peak. The phase transition at about  $-40^\circ\text{C}$  separate the low temperature phase and high temperature phase of the DJ  $n=3$  perovskites. **e**, Temperature dependent of ACI  $n=3$  powder diffraction spectra of the (101 and 111) plane. **f and g** Corresponding temperature and full-width-at-half-maximum (FWHM) evolution of the out-of-plane (squares) and in-plane (circles) lattice parameters. **h and i**, Temperature dependent of RP  $n=3$  powder diffraction spectra of the (060) (**h**) and (111) (**i**) plane. **j**, Corresponding lattice parameter for the out-of-plane and in-plane diffraction peak.



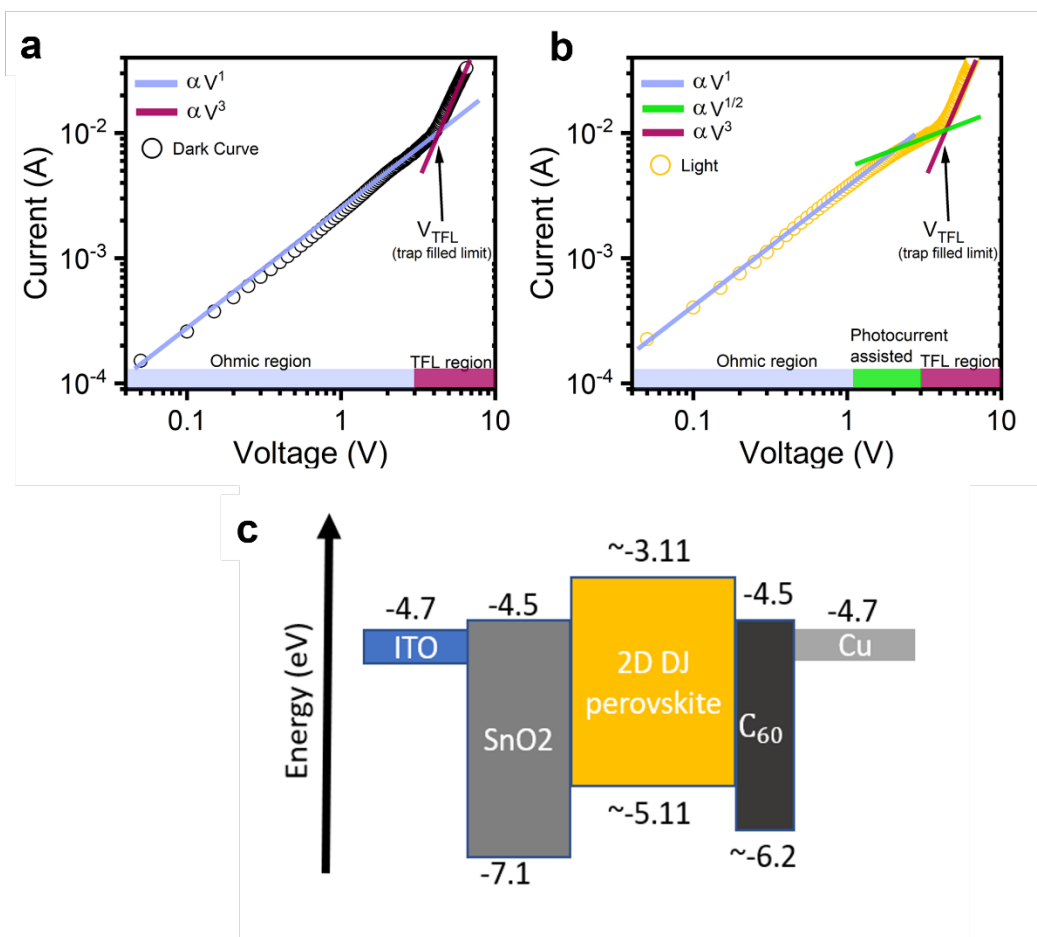
**Supplementary Fig. 4 | Evolution of the structure of the Alternating-Cation (GA)  $\text{MA}_2\text{Pb}_2\text{I}_7$  (ACI  $n=2$ ) and Alternating-Cation (GA)  $\text{MA}_3\text{Pb}_3\text{I}_{10}$  (ACI  $n=3$ ) perovskite under light illumination. **a** and **b** Structure of the ACI  $n=2$  (**a**) and ACI  $n=3$  (**b**) perovskites.<sup>4</sup> The unit cell is indicated by the dashed line. **c** and **d**, Diffraction spectra before and after 51 minutes light illumination for  $n=2$  (**c**) and  $n=3$  (**d**). **e** and **f**, Evolution of the lattice parameters as a function of illumination time for  $n=2$  (**e**) and  $n=3$  (**f**).**



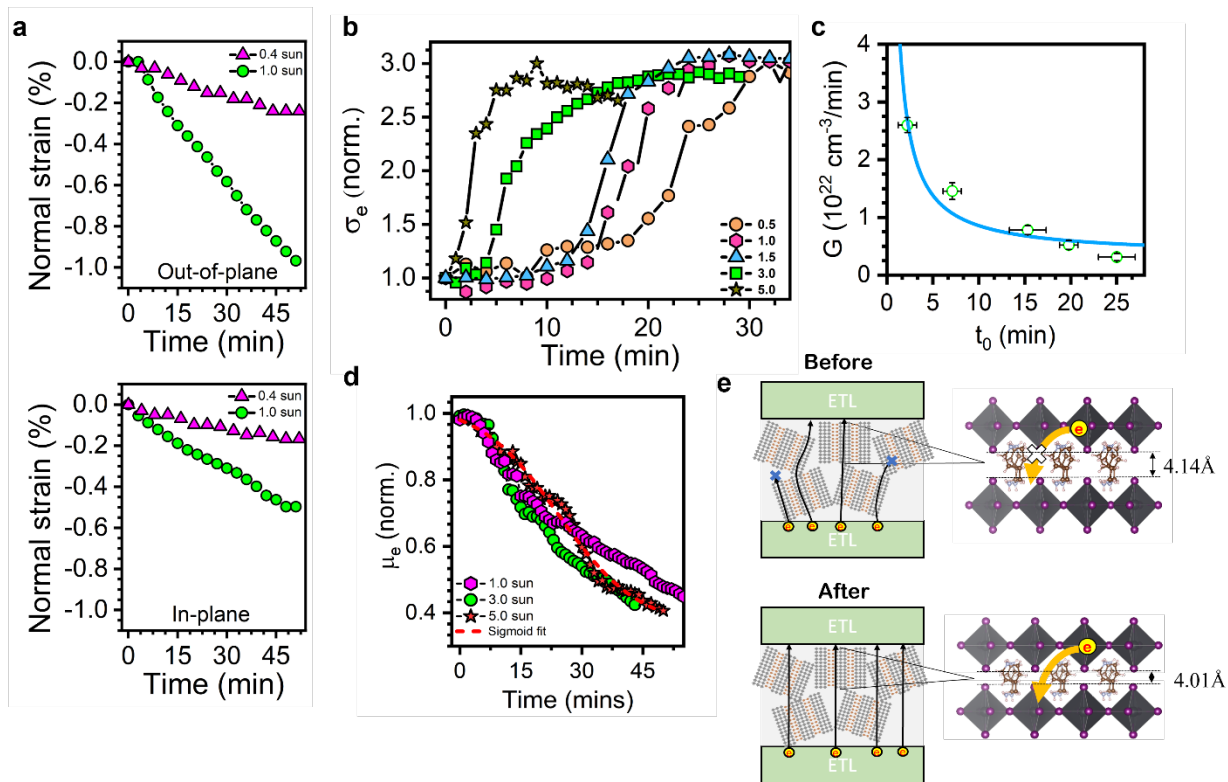
**Supplementary Fig. 5 | Evolution of the structure of Ruddlesden-Popper  $(\text{BA})_2\text{MA}_2\text{Pb}_3\text{I}_{10}$  (RP  $n=3$ ) perovskites under light illumination. **a**, Structure of the RP  $n=3$  perovskites.<sup>1</sup> The unit cell is indicated by the dashed line. **b**, Example of a typical GIWAXS pattern. **c**, Diffraction spectra before (solid) and after 51 minutes light illumination (dash).**



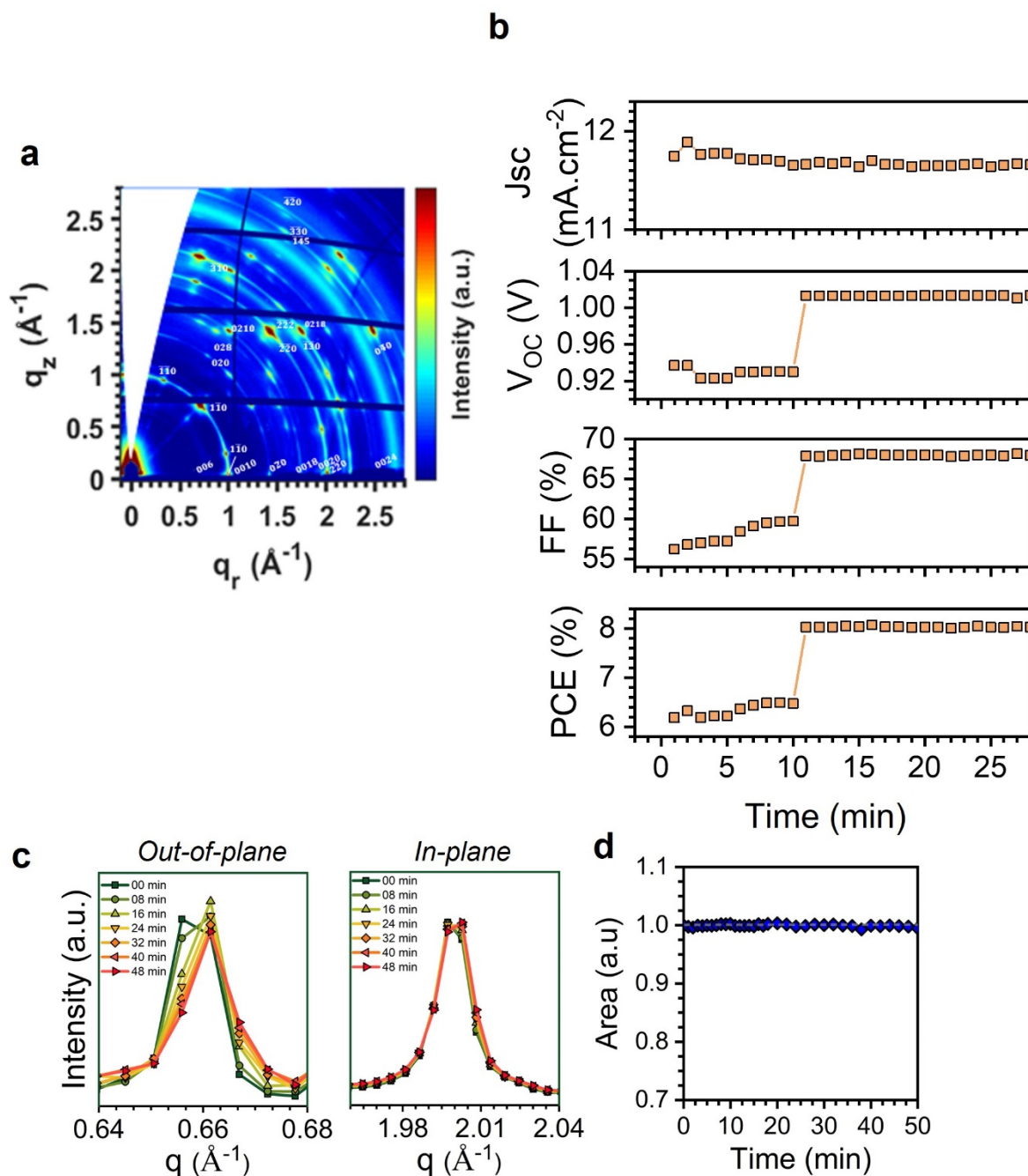
**Supplementary Fig. 6 | X-ray photoelectron emission spectroscopy of 3D and 2D perovskite under light and DJ lattice structure as a function of the charge injected in the lattice obtained from first principal calculations. a**, Evolution of the  $\text{Pb}^{2+}$  (left) and  $\text{I}^-$  (right) photoelectron emission for  $\text{MAPbI}_3$  perovskite film under light illumination. **b**, Evolution of the  $\text{Pb}^{2+}$  (left) and  $\text{I}^-$  (right) photoelectron emission for DJ  $n=3$  perovskite film under light illumination. **c**, Calculated strain as a function of the charge injected in the lattice obtained from first principle. **d**, Changes in the in-plane and out-of-plane Pb-I-Pb angle (octahedra tilting) for the DJ, ACI and RP perovskites as a function of the injected charge. (Right-hand side panel) Schematic of the Pb-I-Pb angle.



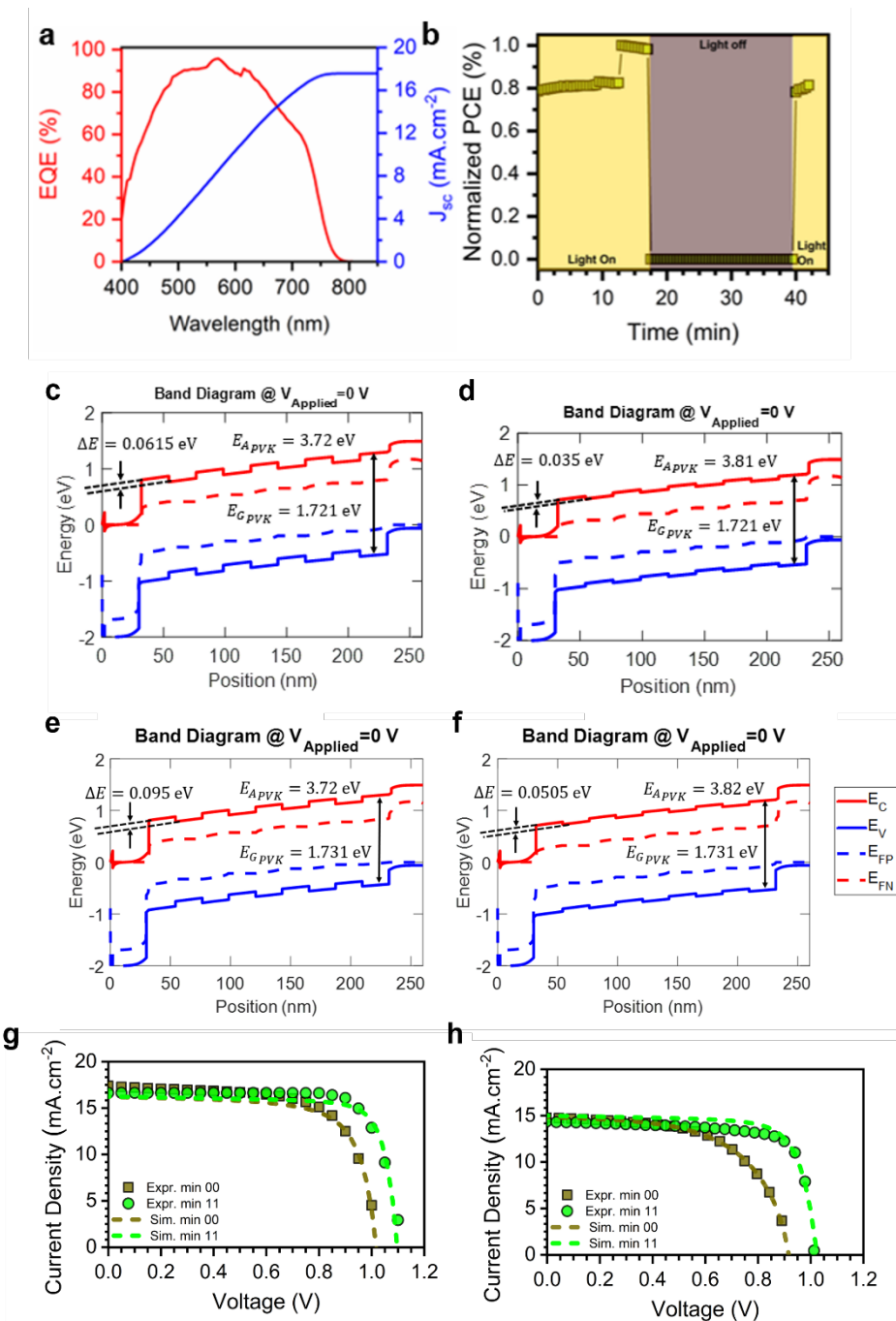
**Supplementary Fig. 7 | Dark and illuminated current-voltage traces for electron only device.** **a**, Current-voltage curve for electron only device in the dark. **b**, Current-voltage curve for electron only device under light. Each panel is marked with the Ohmic, space charge limited photocurrent (photocurrent assisted), and trap filled limit region. **c**, Symmetrical energy band alignment for an electron only device



**Supplementary Fig. 8 | Intensity dependent GIWAXS and SCLC measurement.** **a**, Evolution of the out-of-plane (top panel) and in-plane (bottom panel) normal strain as a function of light illumination for 0.4 suns and 1.0 suns, respectively. **b**, Flux dependent conductivity as a function of light illumination time. **c**, fitted percolation time threshold as a function of photocarrier generation rate. **d**, Conductivity as a function of relaxation time for different light intensities. **e**, Schematic of the before and after light illumination for the charge transport mechanism.



**Supplementary Fig. 9 | GIWAXS characterization of DJ thin film and thin-film solar cell device under continuous light illumination. a**, Grazing incidence wide-angle x-ray scattering patterns of the thin films solar cell device. Method of indexing can be found in ref [42] **b**, Device performances as a function of illumination time. **c**, Angular-integrated spectra for the out-of-plane and the in-plane as a function of illumination time. **d**, Evolution of total diffraction area under illumination.



**Supplementary Fig. 10 | Device characterization and drift diffusion device modeling. a,** External quantum efficiency for the DJ  $n=4$  perovskite solar cell. **b,** Normalized power conversion efficiency for DJ  $n=4$  perovskite device. Cycle plot contains 17 mins of light on and then 23 mins of light off and then 3 mins of light on again. **c,e,** Energy diagram along the perovskite thin films cross-section before light illumination for DJ  $n=4$  (**c**) and ACI  $n=3$  (**e**). **d,f,** Energy diagram after 11 minutes illumination for DJ  $n=4$  (**d**) and ACI  $n=3$  (**f**). **g,h,** Comparison of the experimental and simulated current-voltage characteristics at 0 min and after 11 minutes under continuous light illumination for DJ  $n=4$  (**g**) and ACI  $n=3$  (**h**).